# UC Davis

UC Davis Previously Published Works

Title

Transfer of nuclear and ribosomal material from Sox10-lineage cells to neurons in the mouse brain

Permalink

https://escholarship.org/uc/item/6cg561tn

Journal

Journal of Experimental Medicine, 220(7)

ISSN

0022-1007

Authors

Mayrhofer, Florian
Hanson, Angela M
Navedo, Manuel F
et al.

Publication Date

2023-07-03

DOI

10.1084/jem.20221632

Peer reviewed

## BRIEF DEFINITIVE REPORT

# Transfer of nuclear and ribosomal material from Sox10-lineage cells to neurons in the mouse brain

Florian Mayrhofer[1], Angela M. Hanson[1], Manuel F. Navedo[3], Yang K. Xiang[3,4], Athena M. Soulika[1,5], Wenbin Deng[1,2,6], and Olga V. Chechneva[1,2]

**Material transfer is an essential form of intercellular communication to exchange information and resources between cells. Material transfer between neurons and from glia to neurons has been demonstrated to support neuronal survival and activity. Understanding the extent of material transfer in the healthy nervous system is limited. Here we report that in the mouse central nervous system (CNS), neurons receive nuclear and ribosomal material of Sox10-lineage cell (SOL) origin. We show that transfer of SOL-derived material to neurons is region dependent, establishes during postnatal brain maturation, and dynamically responds to LPS-induced neuroinflammation in the adult mouse brain. We identified satellite oligodendrocyte–neuron pairs with loss of plasma membrane integrity between nuclei, suggesting direct material transfer. Together, our findings provide evidence of regionally coordinated transfer of SOL-derived nuclear and ribosomal material to neurons in the mouse CNS, with potential implications for the understanding and modulation of neuronal function and treatment of neurological disorders.**

## Introduction

Neurons are long-living cells that perform high energy-consuming functions such as firing action potential, axonal transport, protein synthesis, release, and uptake of neurotransmitters to process and transmit information through electrical and chemical signals, thought to be the basis for learning, memory, and behavior (Attwell and Laughlin, 2001; Harris and Attwell, 2012; Shulman et al., 2004). Material transfer from neuron to neuron and glia to neuron plays a critical role in the modulation of neuronal activity and fulfilling energy demands of neurons (Chamberlain et al., 2021; Frühbeis et al., 2013; Pearson et al., 2016). Transfer of cytoplasmic and membrane-bound molecules through tunneling nanotubes has been reported between photoreceptors in vitro and in vivo and demonstrated to restore visual function after photoreceptor precursor transplantation into the diseased neuroretina (Kalargyrou et al., 2021; Ortin-Martinez et al., 2021; Pearson et al., 2016). To a bigger part, extracellular vesicles have been shown to transfer molecules or pathogenic proteins between glia and neurons (Asai et al., 2015; Frühbeis et al., 2013; Guo et al., 2020; Luarte et al., 2020; Patel and Weaver, 2021; Rostami et al., 2017). Increase in transfer of ribosome-containing extracellular vesicles from Schwann cells

to injured axons has been demonstrated in the peripheral nervous system (Court et al., 2008; Lopez-Verrilli et al., 2013; Müller et al., 2018; Shakhbazau et al., 2016). Material transfer of RNA- and protein-carrying exosomes from myelinating oligodendrocytes to axons has been shown in vitro and in vivo and demonstrated to enhance axonal energy metabolism after oxidative stress or starvation (Chamberlain et al., 2021; Frühbeis et al., 2013; Frühbeis et al., 2020). While glia-to-neuron material transfer is mostly viewed as a mechanism to support neuronal survival and recovery after injury, understanding the extent of material transfer in the healthy central nervous system (CNS) is limited.

Sox10 is a member of the high-mobility group gene family of transcription factors involved in the regulation of embryonic development and determination of cell fate (Bowles et al., 2000; Kuhlbrodt et al., 1998). In the postnatal and adult CNS, expression of Sox10 is established as a marker of oligodendrocyte-lineage cells, including oligodendrocyte precursor cells (OPC), pre-myelinating and myelinating oligodendrocytes (Kuhlbrodt et al., 1998). While myelination is considered as the main role of Sox10-lineage cells (SOL; Stolt et al., 2002), in the adult brain

.......................................................................................................................................................................................................
[1]Institute for Pediatric Regenerative Medicine, Shriners Children's Northern California, Sacramento, CA, USA;   [2]Department of Biochemistry and Molecular Medicine, School of Medicine, University of California, Davis, Sacramento, CA, USA;   [3]Department of Pharmacology, University of California, Davis, Davis, CA, USA;   [4]Northern California Health Care System, Mather, CA, USA;   [5]Department of Dermatology, University of California, Davis, Sacramento, CA, USA;   [6]School of Pharmaceutical Sciences, Shenzhen Campus of Sun Yat-sen University, Guangdong, China.

Correspondence to Olga V. Chechneva: chechneva@gmail.com;   Florian Mayrhofer: fmayrhofer@gmail.com.

only about 1% of OPC become myelinating oligodendrocytes (Hughes et al., 2013), as other functions of SOL in the CNS remain unclear.

In this study, we report nuclear and ribosomal material transfer from SOL to neurons in the mouse CNS and provide evidence of coordinated nuclear interaction between satellite oligodendrocytes and neurons.

## Results and discussion

### Neurons receive SOL-derived nuclear and ribosomal material

Using the Cre-LoxP system for the expression of ribosomal Rpl10a fused to enhanced GFP (Rpl10a-EGFP; Liu et al., 2014) or inner nuclear membrane protein Sun1 fused to superfolder GFP (Sun1-sfGFP; Mo et al., 2015), in the oligodendrocyte-lineage cell *Sox10-Cre* mouse line (Philips et al., 2021; Zhang et al., 2020), we unexpectedly found the presence of nuclear and ribosomal reporters not only in oligodendrocyte-lineage cells but also in neuronal cell bodies throughout the entire adult CNS (Fig. 1, A–C; and Fig. S1, A–D). Cell quantification in the mouse brain using immunohistochemistry showed regional differences in the distribution of reporter-positive neurons between cortex, striatum, and thalamus (Fig. 1 F). Analysis by fluorescence-activated nuclei sorting of nuclei isolated from the cortex or thalamus showed similar results (Fig. S1, E and F). The proportion of reporter-positive Olig2^{+} oligodendrocyte-lineage cells was consistently high in all examined areas (Fig. 1 G). In control adult *Sox10-Cre:EYFP* reporter mice expressing unfused enhanced YFP (EYFP; Srinivas et al., 2001), we detected strong expression of EYFP reporter in oligodendrocyte-lineage cells (Fig. 1, D and E). In contrast to nuclear and ribosomal reporter mice, only few weakly fluorescent neurons were found in control *Sox10-Cre:EYFP* mice (6.8 ± 1.5% in the cortex, 1.7 ± 0.9% in the thalamus, and 2.0 ± 1.0% in the striatum; Fig. 1, D–F), as described earlier (Kougioumtzidou et al., 2017). In the cortex, reporter-positive neurons were predominantly glutamatergic (Fig. 1, H and I). Some reporter-positive astrocytes were detected in the hippocampus and deep gray matter, including striatum, thalamus, and hypothalamus (Fig. S1 G). We did not find reporter-positive microglia, a dominant phagocytic cell type in the CNS (Fig. S1 G; Damisah et al., 2020).

Cre-expressing oligodendrocytes have been demonstrated to release Cre protein–containing exosomes in vitro that were internalized by neurons after in vivo transplantation (Frühbeis et al., 2013). To test for misexpression of reporter protein in neurons due to unexpected transient expression or transfer of Cre, we crossed *Sox10-Cre* mice with *Sun1-sfGFP* nuclear reporter mice carrying the inducible diphtheria toxin (DT) receptor (*iDTR*) transgene. In the resulting offspring, Cre-dependent expression of iDTR mediates cell lineage ablation after DT administration (Buch et al., 2005). Stereotaxic injection of DT to the cerebral cortex or thalamus of *Sox10-Cre:iDTR Sun1-sfGFP* double reporter mice resulted in specific ablation of Olig2^{+} oligodendrocyte-lineage cells at the injection site 3 d after treatment (Fig. 2, A–C). The presence of neurons at the injection site with location and numbers similar to neurons in control *Sox10-Cre:Sun1-sfGFP* mice (Fig. 2, B, D, and E) supports the conclusion

that neurons in *Sox10-Cre* mice do not express reporter protein. While we found no decrease in the numbers and mean fluorescence intensity of reporter-positive neurons at 3 d after DT treatment (Fig. 2, E and F), likely due to the short time window after SOL ablation, rapid SOL repopulation (Đặng et al., 2019) needs to be considered when investigating the long-term effects of SOL-neuron material transfer using depletion models.

Using other available nuclear and ribosomal reporter constructs in *Sox10-Cre* mice, we detected similar regional distribution of neurons positive for core histone H2B fused to mCherry (H2B-mCherry; Fig. 2, G and I; Peron et al., 2015; Roh et al., 2017), ribosomal Rpl22 fused to hemagglutinin (Rpl22-HA; Fig. 2 H; Sanz et al., 2009), and nuclear pore complex component RanGAP1 fused to mCherry (RanGAP1-mCherry; Fig. 2 J; Roh et al., 2017).

Supporting our findings on SOL-derived material transfer, abundant accumulation of ribosomal Rpl10a-EGFP was found in neurons in another oligodendrocyte-lineage cell reporter mouse line *PDGFRα-Cre:Rpl10a-EGFP* (Fig. S2, A, C, and D). No EYFP^{+} neurons were found in control *PDGFRα-Cre:EYFP* mice (Fig. S2, B–D). Of note, *PDGFRα-Cre:Rpl10a-EGFP* mice displayed pathological phenotype, including slow growth and seizures. In possible relation to overexpression of ribosomal reporter Rpl10a-EGFP, runty appearance and craniofacial abnormalities were observed in *Sox10-Cre:Rpl10a-EGFP* and *Sox10-Cre:Rpl10a-EGFP H2B-mCherry* mice (Fig. S2, E and F). During embryonic development, Sox10^{+} migrating neural crest cells give rise to craniofacial connective tissue, cartilage, and bone (Bronner and Simões-Costa, 2016). Craniofacial abnormality and developmental delay are common characteristics of ribosomopathies, caused by alterations in the structure or function of ribosomal components (Achilleos and Trainor, 2015; Farley-Barnes et al., 2019; Shi et al., 2017). Further characterization of these mice is needed to understand the relevance between Rpl10a-EGFP expression in SOL, craniofacial abnormality, and related developmental disorders.

### SOL-neuron material transfer in the postnatal mouse brain

Most CNS neurons are generated before birth (Antón-Bolaños et al., 2018; Götz and Huttner, 2005; Rakic, 2009). Early after birth, the CNS undergoes rigorous remodeling with formation of synaptic connections and neural circuits, growth of dendrites, primary myelination, and neuronal specification in the thalamus preceding cortical neuronal specification (Antón-Bolaños et al., 2018; Jernigan et al., 2011; Kroon et al., 2019; López-Bendito and Molnár, 2003; Rice and Barone, 2000; Semple et al., 2013). During late postnatal development, from postnatal day (P) 14 to P30 in the rodent brain, thalamocortical circuit maturation and a refinement of synaptic connections direct the development of cognition and coordinated motor function (Downes and Mullins, 2014; Foran and Peterson, 1992; Mizuno et al., 2018; Paolicelli et al., 2011; Rice and Barone, 2000).

Using *Sox10-Cre:Rpl10a-EGFP* mice, we found a gradual increase in the numbers of reporter-positive Olig2^{+} cells in the cortex, hippocampal dentate gyrus (DG), striatum, and thalamus during early postnatal development from P5 to P14 (Fig. 3, A–G), supporting Olig2 regulatory function upstream of Sox10 expression in OPC, as previously reported (Küspert et al., 2011). At
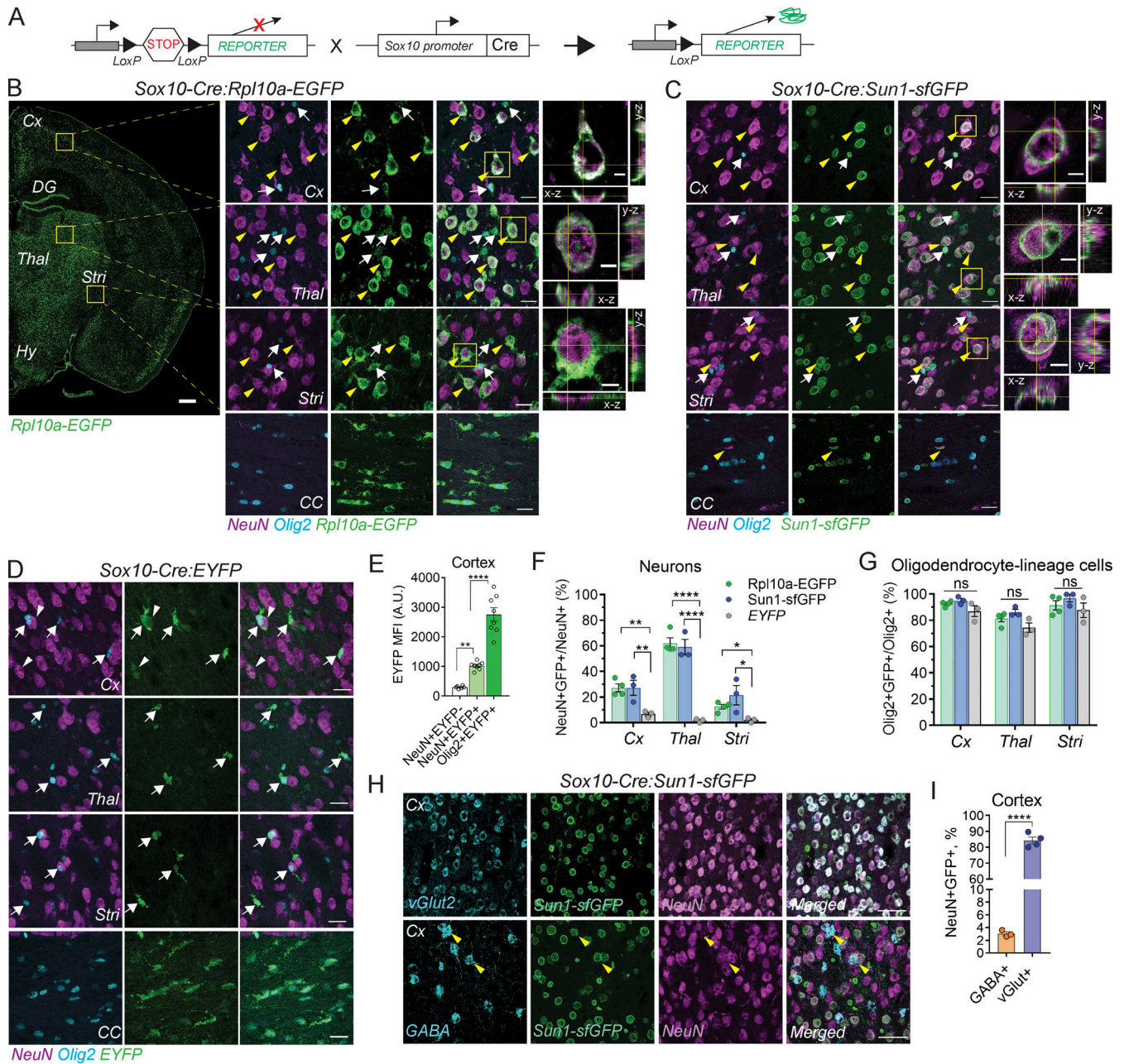
Mayrhofer et al.
Neurons receive material from Sox10-lineage cells

Journal of Experimental Medicine    2 of 15
https://doi.org/10.1084/jem.20221632

Figure 1. **Accumulation of nuclear and ribosomal reporters in neurons in *Sox10-Cre* mice. (A)** Homozygous mice carrying transgene with a loxP-flanked DNA STOP sequence preventing expression of the downstream reporter protein were crossed with *Sox10-Cre* mice to remove the STOP sequence in SOL. **(B and C)** Ribosomal Rpl10a-EGFP or nuclear Sun1-sfGFP reporter was found in oligodendrocyte-lineage cells (arrows) and neurons (yellow arrowheads) in the cortex, thalamus, striatum, and the subcortical white matter corpus callosum of adult *Sox10-Cre:Rpl10a-EGFP* and *Sox10-Cre:Sun1-sfGFP* mice. The region of the yellow box is enlarged and shown as a single plane image with orthogonal projection. **(D)** EYFP reporter protein was found predominantly in oligodendrocyte-lineage cells (arrows) and few weakly fluorescent neurons (arrowheads) in adult *Sox10-Cre:EYFP* mice. **(E)** Quantification of EYFP mean fluorescence intensity (MFI) in neurons and oligodendrocyte-lineage cells in the cortex of adult *Sox10-Cre:EYFP* mice. **(F and G)** Quantification of NeuN$^+$GFP$^+$ neurons and Olig2$^+$GFP$^+$ oligodendrocyte-lineage cells in the cortex, thalamus, and striatum of adult *Sox10-Cre:Rpl10a-EGFP*, *Sox10-Cre:Sun1-sfGFP*, and *Sox10-Cre:EYFP* mice. **(H)** Reporter-positive neurons in the adult mouse cortex were predominantly glutamatergic and rarely GABAergic (arrowheads). **(I)** Quantification of GFP$^+$ glutamatergic and GABAergic neurons in the cortex of adult *Sox10-Cre:Sun1-sfGFP* mice. All data are presented as mean ± SEM. Each circle represents an individual animal in F, G, and I and an individual cell in E. Data are representative of two (H and I) and three (B–G) independent experiments. P values were determined by two-way ANOVA with Bonferroni post hoc test for E–G and unpaired *t* test for I. ns, P > 0.05; *, P < 0.05; **, P < 0.01; ****, P < 0.0001. Scale bars: 500 μm for B; 50 μm for H; 20 μm for enlargements in B, and C and D; 5 μm for orthogonal projections in B and C. A.U., arbitrary units; CC, corpus callosum; Cx, cortex; Hy, Hypothalamus; ns, not significant; Stri, striatum; Thal, thalamus.
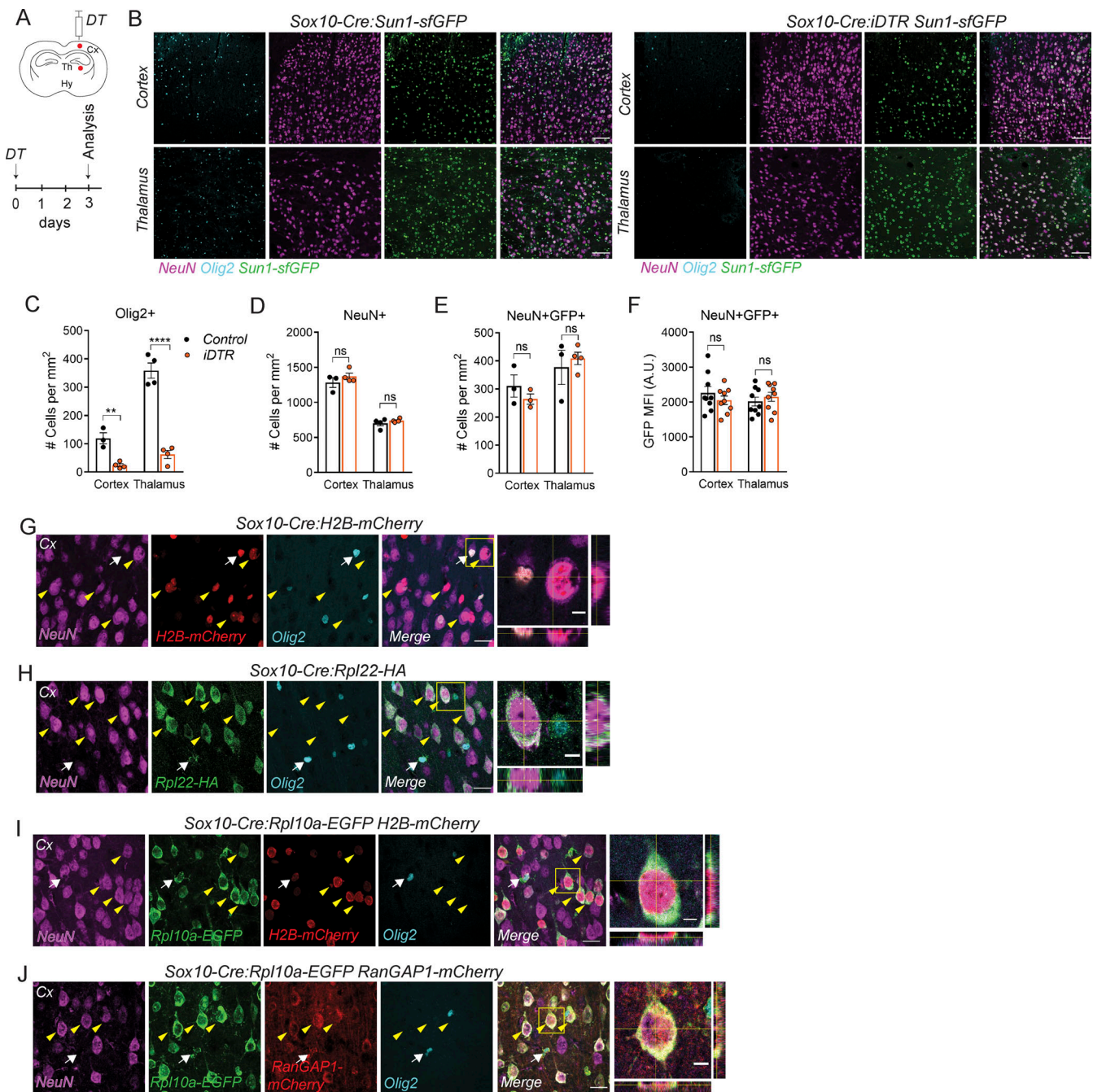
Figure 2. **CNS neurons receive nuclear and ribosomal material from SOL. (A)** 1 ng of DT was injected into the cerebral cortex or thalamus of 8–12-wk-old *Sox10-Cre:iDTR Sun1-sfGFP* and control *Sox10-Cre:Sun1-sfGFP* mice. **(B)** Selective ablation of oligodendrocyte-lineage cells at the injection site in *Sox10-Cre:iDTR Sun1-sfGFP* mice 3 d after DT injection. Neuronal density at the injection site in *Sox10-Cre:iDTR Sun1-sfGFP* mice was indistinguishable from neuronal density in control *Sox10-Cre:Sun1-sfGFP* mice. **(C–E)** Quantification of Olig2+ oligodendrocyte-lineage cells, NeuN+ and NeuN+GFP+ neurons in the cortex or thalamus 3 d after DT injection. **(F)** Quantification of GFP MFI in individual neurons in the cortex or thalamus 3 d after DT injection. **(G–J)** Nuclear and ribosomal reporters in oligodendrocyte-lineage cells (arrows) and selective neurons (arrowheads) in the cortex of adult *Sox10-Cre:H2B-mCherry*, *Sox10-Cre:Rpl22-HA*, *Sox10-Cre:Rpl10a-EGFP H2B-mCherry*, *Sox10-Cre:Rpl10a-EGFP RanGAP1-mCherry* mice. The region of the yellow box is enlarged and shown as a single plane image with orthogonal projection. All data are presented as mean ± SEM. Each circle represents an individual animal in C–E and individual cell in F. Data are representative of two (G–J) and three (B–F) independent experiments. P values were determined by two-way ANOVA with Bonferroni post hoc test. ns, P > 0.05; **, P < 0.01; ***, P < 0.001. Scale bars: 100 µm for B; 20 µm for G–J and 5 µm for the enlargements in G–J. A.U., arbitrary units; CC, corpus callosum; Cx, cortex; HA, hemagglutinin; Hy, Hypothalamus; ns, not significant; Thal, thalamus.
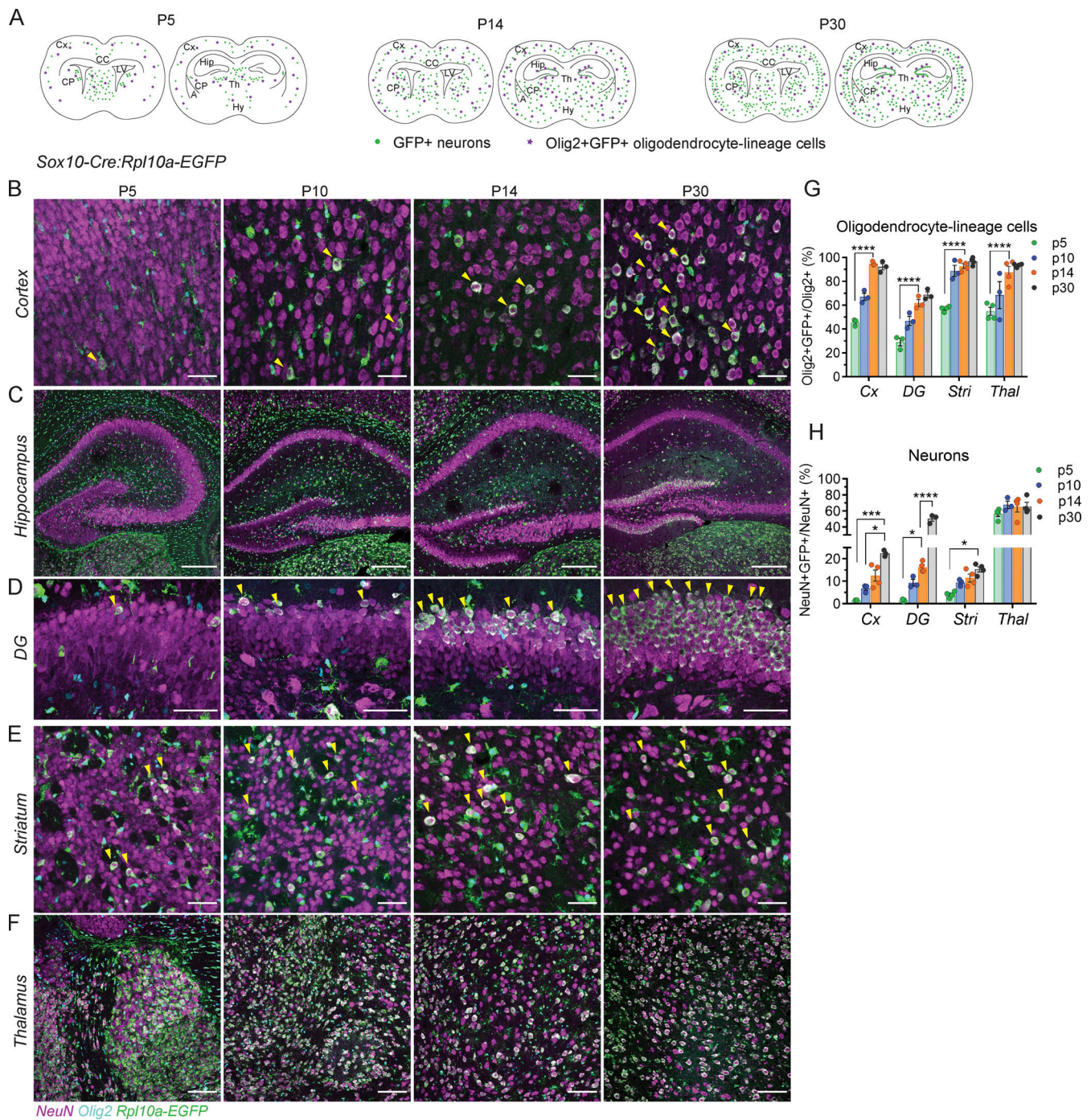
Figure 3. **SOL-neuron material transfer in the postnatal mouse brain. (A)** Schematic representation of regional distribution of nuclear and ribosomal reporter-positive neurons and reporter-positive Olig2+ oligodendrocyte-lineage cells at P5, P14, and P30. **(B–F)** Representative images showing Rpl10a-EGFP+ neurons (arrowheads) and Olig2+ oligodendrocyte-lineage cells in the cortex, hippocampal DG, striatum, and thalamus during postnatal development. **(G and H)** Quantification of Olig2+GFP+ oligodendrocyte-lineage cells and NeuN+GFP+ neurons in the postnatal brain of *Sox10-Cre:Rpl10a-EGFP* mice. All data are presented as mean ± SEM. Each circle represents an individual animal. Data are representative of three independent experiments. P values were determined by one-way ANOVA with Bonferroni post-hoc test. *, P < 0.05; ***, P < 0.001; ****, P < 0.0001. Scale bar: 500 μm for C; 100 μm for F; 50 μm for B, D, and E. A, amygdala; CP, caudate putamen; CC, corpus callosum; Cx, cortex; Hip, hippocampus; Hy, hypothalamus; Th, thalamus.

P14, the numbers of reporter-positive Olig2+ SOL were established in all examined areas (Fig. 3 G). Concurrently, very few reporter-positive neurons were found in the cortex, hippocampal DG, and striatum at P5, but their numbers gradually increased until P30, reaching the numbers found in the mature adult mouse brain (Fig. 1 F and Fig. 3, A–E and H). In contrast, the numbers of reporter-positive neurons in the thalamus remained stable throughout postnatal development and comparable with the numbers found in the adult brain (Fig. 1 F and Fig. 3, A, F, and H). Because the visualization of SOL-neuron

Mayrhofer et al.
Neurons receive material from Sox10-lineage cells

Journal of Experimental Medicine   5 of 15
https://doi.org/10.1084/jem.20221632

material transfer in our system is dependent on expression of Sox10 in oligodendrocyte-lineage cells, it remains unknown whether material transfer is happening to a bigger extend earlier in development. Together, we conclude that SOL-neuron material transfer establishes during postnatal maturation. How SOL-neuron material transfer is regulated during development and its role in brain maturation remains to be determined.

## SOL-neuron material transfer in the adult brain

To study SOL-neuron material transfer in the adult brain, we employed the inducible CreER[T2]/LoxP system. In this system, activation of CreER[T2] recombinase by synthetic estrogen receptor ligand tamoxifen (TAM) allows controlled expression of reporter protein (Fig. 4 A). We used oligodendrocyte-lineage cell mouse line *Sox10-iCreER[T2]* (McKenzie et al., 2014; Zhang et al., 2020). After TAM injection to nuclear *Sox10-iCreER[T2]:Sun1-sfGFP* or ribosomal *Sox10-iCreER[T2]:Rpl10a-EGFP* reporter mice, in addition to reporter-positive oligodendrocyte-lineage cells, we found Sun1-sfGFP[+] or Rpl10a-EGFP^{+} neurons in specific areas of the adult mouse brain: cortical layers 2–3 and 6, DG, septum, and amygdala (Fig. 4, B–D; and Fig. S3 A). Single reporter-positive neurons were detected in the hippocampal CA1-3 pyramidal layer (Fig. S3 A).

Cre protein was selectively expressed in oligodendrocyte-lineage cells, and we did not find reporter-positive neurons immunoreactive for Cre (Fig. 4 E). Cell quantification using immunohistochemistry showed that around 97% of Olig2^{+} cells in the cortex of *Sox10-iCreER[T2]:Sun1-sfGFP* mice expressed fluorescent reporter at 4, 8, and 30 d after TAM induction (Fig. 4 F). In contrast, the numbers of reporter-positive neurons found in the cortex at 4 d after TAM were reduced at 8 d and remained stable at 30 d after TAM (Fig. 4, G and H), which may be explained by transient acute increase in material transfer in response to TAM-induced cellular stress (Denk et al., 2015) and the documented rapid protein turnover in neurons, with the half-life of 6 d for Sun1 (Buchwalter et al., 2019) and 6–11 d for ribosomal proteins (Dörrbaum et al., 2018). During examination of reporter-positive neurons in the cortex of *Sox10-iCreER[T2]:Sun1-sfGFP* mice, we frequently found satellite Olig2^{+}Sun1-sfGFP[+] SOL forming nuclear pairs with reporter-positive neurons (Fig. 4, C and I). The numbers of Sun1-sfGFP[+] SOL-neuron nuclear pairs positively correlated with the numbers of reporter-positive neurons (Fig. 4, I and J), suggesting a possible function in SOL-derived material transfer to neurons.

## SOL-neuron material transfer responds to neuroinflammation

Reactive gliosis and neuroinflammation trigger and perpetuate pathogenesis in a variety of genetic and age-related neurodegenerative disorders associated with aggregation and spreading of pathogenic proteins in neurons, including Alzheimer's, Huntington's, Parkinson's disease, and amyotrophic lateral sclerosis (Batista et al., 2019; Heppner et al., 2015). LPS, a major component of the outer membrane of Gram-negative bacteria, has been widely used to model neuroinflammation, and LPS was found in the postmortem human brain tissue of patients with progressive accumulation of protein aggregates (Batista et al., 2019; Brown, 2019; Zhan et al., 2016; Zhang et al., 2009).

Systemic administration of LPS causes rapid pro-inflammatory activation of microglia and lasting neurotoxic reactive astrocytes in the CNS (Hasel et al., 2021; Hoogland et al., 2015; Liddelow et al., 2017; Zamanian et al., 2012). To investigate the response of SOL-neuron material transfer to neuroinflammation, we i.p. injected LPS or saline as control to adult *Sox10-iCreER[T2]:Sun1-sfGFP* and *Sox10-iCreER[T2]:Rpl10a-EGFP* reporter mice 3 d after TAM (Fig. 4 K). As described earlier, LPS administration resulted in microglia and astrocyte activation (Fig. 4, L–N; Hasel et al., 2021; Kloss et al., 2001; Liddelow et al., 2017; Zamanian et al., 2012). At 24 h after LPS injection, the numbers of microglia increased in the cortex and microglia appeared with thick processes displaying reactive phenotype (Fig. 4, L and M; Jonas et al., 2012). Microglia numbers returned to control level at 5 d after LPS injection (Fig. 4 M). Hypertrophic reactive astrocytes and astrogliosis assessed by GFAP immunoreactivity were evident at 24 h and persisted at 5 d after LPS administration (Fig. 4, L and N). Acute systemic inflammation triggers proteomic and metabolic changes causing sickness behavior, including fever, lethargy, and hypophagia (Kealy et al., 2020; Mittli et al., 2023). Concurrently, at 24 h after LPS, we found a reduction in the numbers of cortical neurons positive for nuclear reporter Sun1-sfGFP compared to saline-treated control (Fig. 4, L and O). In contrast, increase in numbers of Sun1-sfGFP^{+} neurons compared to saline-treated control was found after recovery from acute response, at 5 d after LPS, in association with early chronic neuroinflammation (Fig. 4, L and O). Similar changes were observed in numbers of Sun1-sfGFP[+] SOL-neuron nuclear pairs in the cortex (Fig. 4 P). No changes in the numbers of reporter-positive oligodendrocyte-lineage cells were found in the cortex at 24 h or 5 d after LPS injection (Fig. 4 Q). In *Sox10-iCreER[T2]:Rpl10a-EGFP* ribosomal reporter mice, changes in numbers of Rpl10a-EGFP^{+} neurons in response to LPS were less prominent (Fig. S3, B and C). We conclude that SOL-neuron material transfer dynamically responds to LPS-induced neuroinflammation. How SOL-neuron material transfer may be regulated by microglia and/or astrocyte reactivity and involved in acute and chronic response to neuroinflammation need to be further investigated.

## Satellite SOL-neuron nuclear pairs in the adult mouse brain

Satellite oligodendrocytes are uniquely positioned in intimate contact with the neuronal soma and have been shown to provide metabolic support to neurons, protect neurons from apoptosis, buffer extracellular potassium, and can be myelinating (Battefeld et al., 2016; Kruger and Maxwell, 1966; Takasaki et al., 2010; Taniike et al., 2002). Given the close positioning of satellite SOL and reporter-positive neurons, we examined SOL-neuron nuclear pairs as possible site of material transfer. In SOL-neuron nuclear pairs found in the cortex of nuclear reporters *Sox10-iCreER[T2]:Sun1-sfGFP* and *Sox10-Cre:Rpl10a-EGFP H2B-mCherry* mice, we observed dense chromatin in satellite SOL compared to dispersed chromatin of neuronal nucleus (Fig. 5 A and Fig. S3 D). SOL-specific proteins, such as Cre recombinase and Olig2, were confined to SOL (Fig. 5 B). Satellite SOL in reporter-positive SOL-neuron nuclear pairs in the cortical layers 2–3 of adult *Sox10-iCreER[T2]:Sun1-sfGFP* mice were
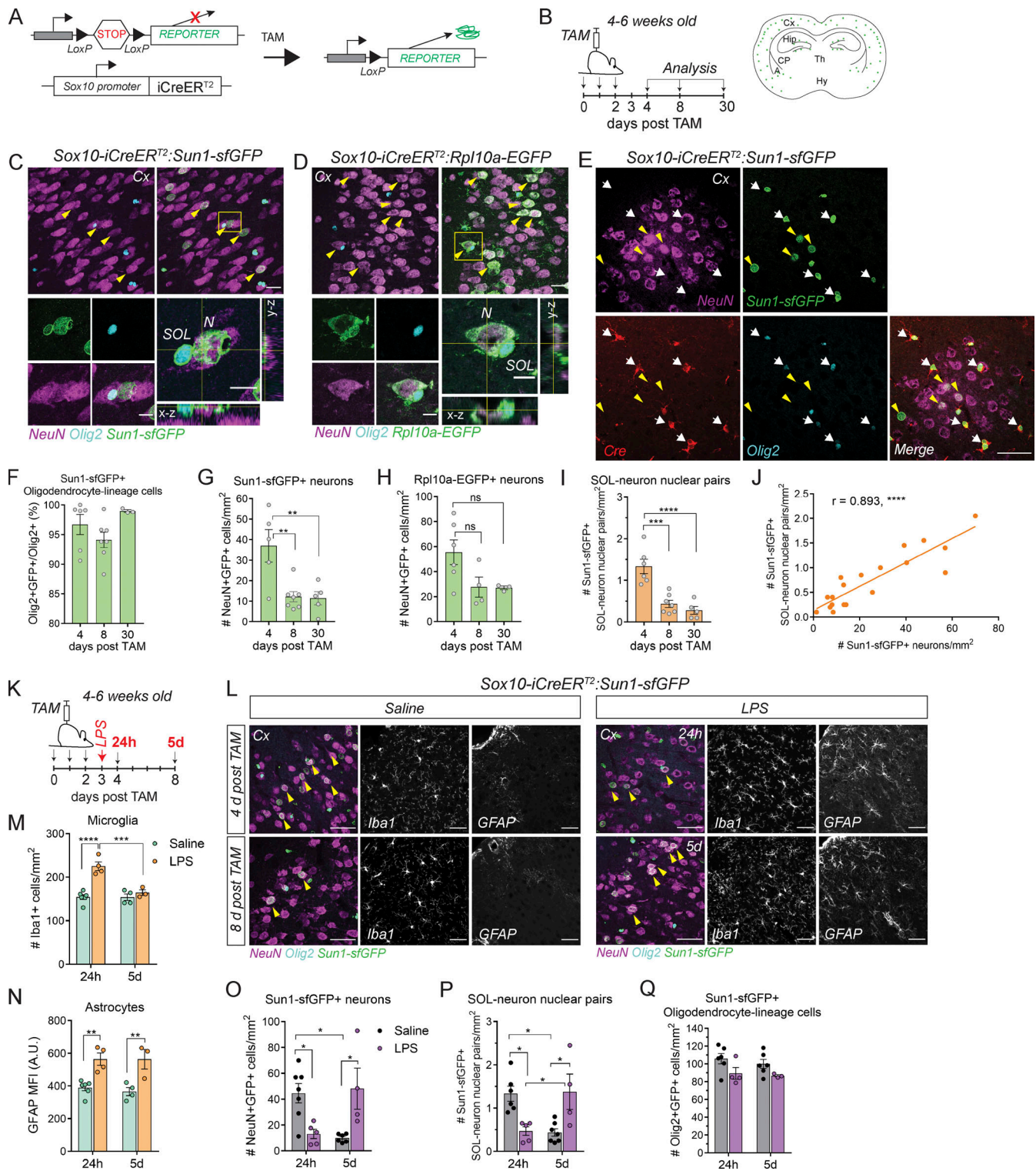
Mayrhofer et al.
Neurons receive material from Sox10-lineage cells

Journal of Experimental Medicine 6 of 15
https://doi.org/10.1084/jem.20221632

Figure 4. **SOL-neuron material transfer in the adult mouse brain. (A)** *Sox10-iCreER[T2]* mice carrying *Sun1-sfGFP* or *Rpl10a-EGFP* reporter transgene with an upstream loxP-flanked DNA STOP sequence were used to induce nuclear or ribosomal reporter expression in Sox10-expressing cells by injection of TAM. **(B)** Experimental timeline and schematic of regional distribution of reporter-positive neurons at 4 d after TAM injection. **(C and D)** Reporter-positive NeuN+ neurons (arrowheads) in cortical layers 2–3 of *Sox10-iCreER[T2]:Sun1-sfGFP* or *Sox10-iCreER[T2]:Rpl10a-EGFP* mice at 4 d after TAM. Note the close positioning of SOL and reporter-positive neuronal nuclei (yellow box). The region of the yellow box is enlarged and shown as maximum intensity projection for individual channels and single plane image with orthogonal projection. **(E)** Cre expression was specific to Olig2+ SOL (arrows) in the cortex of *Sox10-iCreER[T2]:Sun1-sfGFP* mice. No Cre expression was detected in reporter-positive neurons (arrowheads). **(F)** Quantification of reporter-positive Olig2+ SOL in the cortex of *Sox10-iCreER[T2]:Sun1-sfGFP* mice at 4, 8, and 30 d after first TAM injection. **(G and H)** Quantification of reporter-positive NeuN+ neurons in the cortex of *Sox10-iCreER[T2]:Sun1-sfGFP* or *Sox10-iCreER[T2]:Rpl10a-EGFP* mice at 4, 8, and 30 d after first TAM injection. **(I)** Quantification of Sun1-sfGFP+ SOL-neuron nuclear pairs in the cortex of *Sox10-iCreER[T2]:Sun1-*

*sfGFP* mice at 4, 8, and 30 d after first TAM injection. **(J)** Positive correlation between the numbers of Sun1-sfGFP⁺ neurons and SOL-neuron nuclear pairs in the cortex after TAM injection determined by Pearson correlation analysis. **(K)** LPS (4 mg/kg) or saline were i.p. injected to 4–6-wk-old transgenic mice 3 d after TAM to induce systemic inflammation. **(L)** Sun1-sfGFP⁺ neurons (arrowheads), Iba1⁺ microglia, and GFAP⁺ astrocytes in the cortex of *Sox10-iCreER^T2^:Sun1-sfGFP* mice at 24 h and 5 d after saline or LPS injection. **(M)** Quantification of Iba1⁺ microglia numbers in the cortex after saline or LPS injection. **(N)** Quantification of GFAP MFI in astrocytes in the cortex after saline or LPS injection. **(O–Q)** Quantification of reporter-positive NeuN⁺ neurons, SOL-neuron nuclear pairs and oligodendrocyte-lineage cells in the cortex at 24 h and 5 d after LPS injection. All data are presented as mean ± SEM. Each circle represents an individual animal. Data are representative of three independent experiments. P values were determined by one-way ANOVA with Bonferroni post hoc test. ns, P > 0.05; *, P < 0.05; **, P < 0.01; ***, P < 0.001; ****, P < 0.0001. Scale bar: 50 µm for E and L; 25 µm for C and D and 10 µm for enlargements in C and D. A, amygdala; A.U., arbitrary units; CP, caudate putamen; Cx, cortex; Hip, hippocampus; Hy, hypothalamus; N, neuron; ns, not significant; Th, thalamus.

immunoreactive for pan oligodendrocyte-lineage cell markers Olig2 and Sox10, and OPC marker NG2 (Fig. 5, A, C, and E; Barateiro and Fernandes, 2014; Rivers et al., 2008). About 60% of satellite SOL were positive for OPC marker PDGFRα and 40% expressed CC1 (Fig. 5, C and E), a marker of postmitotic oligodendrocytes (Hill et al., 2014). None of these satellite SOL expressed myelin basic protein (Fig. 5, D and E), suggesting that satellite SOL in reporter-positive SOL-neuron nuclear pairs are not myelinating oligodendrocytes.

Super-resolution confocal imaging of inner nuclear membrane component Sun1 in the cortex of *Sox10-iCreER^T2^:Sun1-sfGFP* mice confirmed close positioning of satellite SOL and neuronal nuclei in SOL-neuron nuclear pairs (Fig. 5 F and Video 1). To visualize the ultrastructure of SOL-neuron nuclear pairs and their plasma membrane contact site, we performed transmission electron microscopy (TEM) in the cortex and thalamus of adult *Sox10-Cre:Rpl10a-EGFP* mice. Neurons were identified by large round euchromatic nucleus and pale cytoplasm, nuclei of satellite SOL appeared with dense rim of heterochromatin and ruffled edges, as previously described (Nahirney and Tremblay, 2021). In addition to satellite SOL-neuron pairs that were separated by plasma membrane (Fig. S3, E and F), as has been previously shown (Battefeld et al., 2016; Nahirney and Tremblay, 2021; Takasaki et al., 2010), we found SOL-neuron nuclear pairs with loss of plasma membrane integrity between nuclei (Fig. 5, G–I). In these pairs, SOL and neuronal nuclei were positioned within 250–1,000 nm distance range. Intact plasma membrane continued outlining SOL and neuronal cell bodies (Fig. 5 H). Some neurons extended a protrusion embracing the body of SOL (Fig. 5, G and H). Organelles of SOL appeared shifted away from the SOL-neuron contact site. Mitochondria were found in internuclear space close to the neuronal nucleus. The presence of vesicles and free ribosomes in the SOL-neuron internuclear space suggests that material can be transferred directly between nuclei without passing the plasma membrane. Fusion and donation of genetic material to neurons have been reported in the mouse and human brain after stem cell transplantation and are especially common between cerebellar Purkinje neurons (Alvarez-Dolado et al., 2003; Martínez-Cerdeño et al., 2017; Weimann et al., 2003a; Weimann et al., 2003b). However, strict confinement of SOL-specific proteins to SOL and specificity of Cre and reporter protein expression to SOL argues against complete cell fusion and supports the concept of selective SOL-neuron material transfer. The detailed mechanism of coordinated SOL-neuron nuclear interaction and material transfer remains to be determined.

Together, our study provides evidence of SOL-neuron nuclear and ribosomal material transfer linked to satellite SOL-neuron nuclear interaction in the mouse CNS. While the notion of material transfer from glia to neurons has been previously postulated (Chamberlain et al., 2021; Court et al., 2008; Frühbeis et al., 2013; Lopez-Verrilli et al., 2013; Müller et al., 2018; Shakhbazau et al., 2016), such accumulation of SOL-derived nuclear and ribosomal material in neurons as reported in our study is novel. Our findings suggest that SOL may play a more diverse role in neuronal function, which was previously believed to be largely limited to generation of myelinating oligodendrocytes and axonal support (Morrison et al., 2013). Although neurons likely retain the ability to express nuclear and ribosomal proteins on their own, it is conceivable that SOL-derived material transfer can support neuronal health and activity, and can contribute to neurodegeneration when dysregulated (DiFiglia et al., 1997; Glenner and Wong, 1984; Kosik et al., 1986; Ling et al., 2015; Neumann et al., 2006; Spillantini et al., 1998; Thomas et al., 2017). Determining the regulatory mechanisms and biological function of SOL-neuron material transfer should prove to be an interesting area of research that will open new avenues for exploration of glia-neuron interaction and the development of novel therapeutic interventions for neurological disorders.

## Material and methods
### Mice
Animals were maintained in accordance with the National Institutes of Health (NIH) Guide for the Care and Use of Laboratory Animals. Experimental protocols were approved by the Institutional Animal Care and Use Committee at the University of California, Davis.

All transgenic lines used in this study are commercially available and were obtained from the Jackson Laboratory (see below for Jax stock numbers). Female or male reporter mice were bred with Cre-positive mates. Offspring were genotyped for the presence of the reporter transgene and Cre and screened for absence of germline transmission. Offspring heterozygous for the reporter transgene and Cre-positive were used as reporter animals in this study. Littermates carrying the reporter transgene and either Cre-negative or non-induced CreER^T2^-positive were used as negative control. For DT experiments, *Sun1-sfGFP* mice were crossed to *iDTR* mice. F1 heterozygous offspring were then crossed to generate F2 offspring. F2 male offspring, homozygous for both *Sun1-sfGFP* and *iDTR* alleles were used for
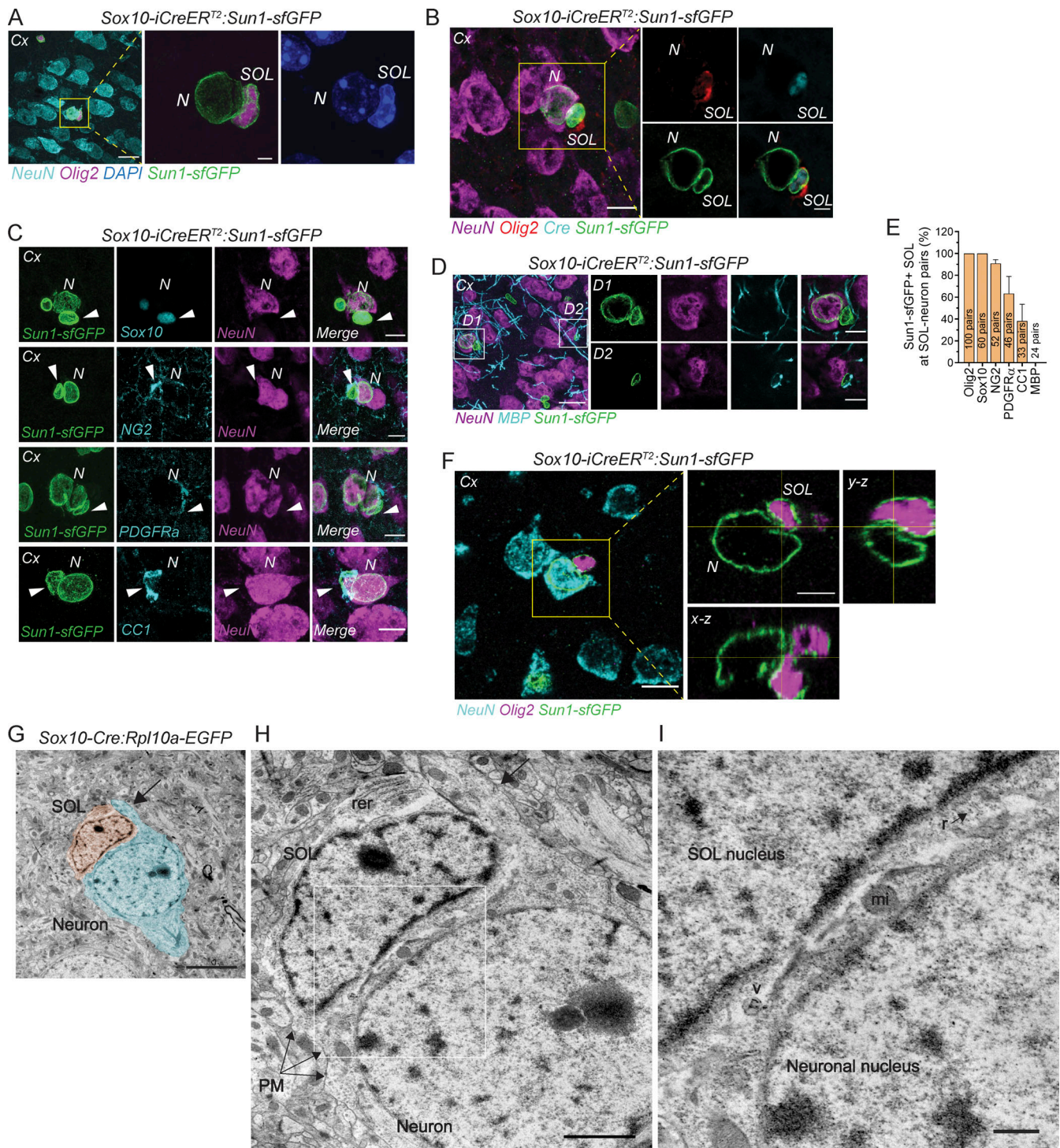
Figure 5. **SOL-neuron nuclear pairs in the adult mouse brain. (A)** Confocal analysis of inner nuclear membrane reporter Sun1-sfGFP revealed SOL-neuron nuclear pairs in the cortex of adult *Sox10-iCreER^T2^:Sun1-sfGFP* mice at 4 d after first TAM injection. Note, dense DAPI-labeled nucleus of SOL and diffuse DAPI-labeled neuronal nucleus in SOL-neuron nuclear pair. **(B)** Cre recombinase (cyan) and Olig2 (red) immunoreactivity were confined to SOL in the cortex of adult *Sox10-iCreER^T2^:Sun1-sfGFP* mice at 4 d after first TAM injection. **(C)** Oligodendrocyte-lineage cell marker expression in SOL (arrowhead) in Sun1-sfGFP⁺ SOL-neuron nuclear pairs in the cortex of adult *Sox10-iCreER^T2^:Sun1-sfGFP* mice. **(D)** MBP-negative satellite SOL in Sun1-sfGFP⁺ SOL-neuron nuclear pair (D1) and MBP⁺ satellite SOL in proximity to Sun1-sfGFP–negative neuron (D2). **(E)** Quantification of cell marker expression in SOL in Sun1-sfGFP⁺ SOL-neuron nuclear pairs. **(F)** Super-resolution image and orthogonal projection of Sun1-sfGFP⁺ SOL-neuron nuclear pair in the cortex of adult *Sox10-iCreER^T2^:Sun1-sfGFP* mice at 4 d after first TAM injection. **(G)** TEM image of SOL-neuron nuclear pair with pseudocoloring to highlight satellite SOL and neuron with body protrusion (arrow) in the cortex of adult *Sox10-Cre:Rpl10a-EGFP* mouse. **(H and I)**. Higher magnification TEM images of G. SOL and neuron were outlined by intact plasma membranes (PM). Loss of plasma membrane integrity was evident between nuclei, with mitochondria (mi), free ribosomes (r), and vesicles (v) present in the internuclear space. Data are representative of two (A–F) and four (G–I) independent experiments. Scale bars: 25 µm for D; 10 µm for A–C, F, D1, and D2; 5 µm for enlargements in A, B, F, and for G; 2 µm for H; 500 nm for I. Cx, cortex; MBP, myelin basic protein; N, neuron; rer, rough endoplasmic reticulum.

breeding with *Sox10-Cre* females to generate offspring heterozygous for the reporter transgenes and Cre-positive. Adult mice used in the study were 6–12-wk-old unless otherwise specified. No genetic backcrosses were performed for this study in our lab.

## Sox10-Cre

B6;CBA-Tg(Sox10-cre)1Wdr/J, Jax stock no. 025807 (N20$^+$ pN2F1) was donated by William Richardson (University College London, London, UK). These mice express a nuclear-targeted Cre recombinase directed by the endogenous *Sox10* promoter/enhancer regions on a PAC transgene.

## Sox10-iCreER$^{T2}$

CBA;B6-Tg(Sox10-icre/ERT2)388Wdr/J, Jax stock no. 027651 was donated by William Richardson (University College London, London, UK). These mice, carrying a transgene with TAM-inducible optimized (improved) Cre recombinase under the control of the mouse Sox10 (SRY [sex determining region Y]-box 10) promoter, express CreER$^{T2}$ in oligodendrocyte-lineage cells.

## PDGFRα-Cre

C57BL/6-Tg(Pdgfra-cre)1Clc/J, Jax stock no. 013148 was donated by Connie Cepko (Harvard Medical School, Howard Hughs Medical Insitute, Boston, MA, USA). These mice carry a Cre recombinase gene 3′ of the PDGFRα promoter linearized in mouse BAC transgene. When bred with mice containing a loxP-flanked sequence of interest, Cre-mediated recombination will result in deletion of the floxed sequence in the offspring.

## EYFP

B6.129X1-*Gt(ROSA)26Sor^tm1(EYFP)Cos*/J, Jax stock no. 006148 was donated by Frank Costantini (Columbia University Medical Center, New York, NY, USA). These mice have a LoxP-flanked STOP sequence followed by the EYFP inserted into the Gt(ROSA)26Sor locus. When bred to mice expressing Cre recombinase, the STOP sequence is deleted and EYFP expression is observed in the Cre-expressing tissues.

## Rpl10a-EGFP

B6;129S4-*Gt(ROSA)26Sor^tm9(EGFP/Rpl10a)Amc*/J, Jax stock no. 024750 was donated by Andrew P. McMahon (University of Southern California, Los Angeles, CA, USA). These mice have a transgene containing cDNA encoding EGFP fused to ribosomal protein unit L10a (Rpl10a) integrated into the Gt(ROSA)26Sor locus. Expression of the EGFP-tagged form of Rpl10a is blocked by a LoxP-flanked STOP fragment (three copies of SV40 polyA) placed between Gt(ROSA)26Sor promoter and the Rpl10a-EGFP sequence. Cre-mediated excision of STOP fragment results in the constitutive expression of the Rpl10a-EGFP fusion gene.

## Sun1-sfGFP

B6.129-Gt(ROSA)26Sor^tm5(CAG-Sun1/sfGFP)Nat/J, Jax stock no. 021039 or 030952 was donated by Jeremy Nathans (Johns Hopkins University, Baltimore, MD, USA) and Margarita Behrens (The Salk Institute, San Diego, CA, USA). These Sun1-tagged mice are used in the INTACT (isolation of nuclei tagged in specific cell types) method for immunopurification of nuclei. Cre-dependent removal of a floxed STOP cassette allows expression of the Sun1 fusion protein at the inner nuclear membrane in targeted cell types.

## iDTR

C57BL/6-Gt(ROSA)26Sor^tm1(HBEGF)Awai/J, Jax stock no. 007900 was donated by Ari Waisman (Johannes Gutenberg University of Mainz, Mainz, Germany). These mice have the transgene encoding simian DTR (from simian *Hbegf*) inserted into the Gt(ROSA)26Sor locus. Widespread expression of DTR is blocked by an upstream LoxP-flanked STOP sequence. The Cre-inducible expression of DTR in these mice renders cells susceptible to ablation following DT administration.

## Rpl10a-EGFP RanGAP1-mCherry

B6;129S6-*Gt(ROSA)26Sor^tm2(CAG-NuTRAP)Evdr*/J, Jax stock no. 029899 was donated by Evan D. Rosen (Beth Israel Deaconess Medical Center and Harvard Medical School, Boston, MA, USA). These mice have a transgene containing cDNA encoding three individual components BirA, biotin ligase recognition peptide–tagged monomeric red fluorescent protein (mCherry) fused to mouse nuclear membrane Ran GTPase activating protein 1 (RanGAP1) and EGFP fused to ribosomal protein Rpl10a integrated into the Gt(ROSA)26Sor locus. Upon exposure to Cre recombinase, the transgene co-expresses three individual components: BirA, biotin ligase recognition peptide–tagged mCherry-RanGAP1, and Rpl10a-EGFP fusion gene.

## Rpl10a-EGFP H2B-mCherry

B6.Cg-*Gt(ROSA)26Sor^tm1(CAG-HIST1H2BJ/mCherry,-EGFP/Rpl10a)Evdr*/J, Jax stock no. 029789 was donated by Evan D. Rosen (Beth Israel Deaconess Medical Center and Harvard Medical School, Boston, MA, USA). These mice have a transgene containing cDNA encoding human histone 1 H2bj gene (*HIST1H2BJ*) fused in-frame to the N-terminus of a monomeric mCherry and EGFP fused in-frame to the N-terminus of mouse 60S ribosomal subunit Rpl10a integrated into the Gt(ROSA)26Sor locus. Upon exposure to Cre recombinase, the transgene co-expresses Rpl10a-EGFP and H2B-mCherry fusion gene.

## H2B-mCherry

B6;129S-*Gt(ROSA)26Sor^tm1.1Ksvo*/J, Jax stock no. 023139 was donated by Karel Svoboda (Janelia Farm Research Campus, Ashburn, VA, USA). These mice have a transgene containing cDNA encoding human histone 1 H2bb gene (*HIST1H2BB*) followed C-terminally by mCherry gene integrated into the Gt(ROSA)26Sor locus. Cre-mediated excision of the STOP fragment results in the constitutive expression of the H2B-mCherry fusion gene. The CNS tissue of H2B-mCherry Cre-negative mice displays mCherry background expression in all cells. As reported by the donating investigator, after exposure to Cre recombinase, the mCherry expression levels in the nucleus are significantly greater than those baseline levels.

## Rpl22-HA

B6J.129(Cg)-*Rpl22^tm1.1Psam*/SjJ, Jax stock no. 029977 was donated by Simon John (The Jackson Laboratory, Bar Harbor, ME, USA).

These mice carry a targeted mutation of the ribosomal protein L22 (*Rpl22*) locus. Prior to Cre recombinase exposure, RiboTag mice express the wildtype Rpl22 protein (15 kD). Cre-mediated excision of the floxed exon 4 enables tissue-selective expression of the downstream HA epitope-tagged exon 4. The resultant 23 kD HA epitope-tagged ribosomal protein (Rpl22-HA) is incorporated into actively translating polyribosomes.

**TAM induction of Cre activity**

TAM (T5648; Sigma-Aldrich) was dissolved at the concentration of 20 mg/ml in corn oil by shaking at 37°C overnight protected from light. 4–6-wk-old mice received three i.p. injections of 80 mg/kg TAM for three consecutive days. We observed Cre-induced recombination in non-injected Cre+ mice that were housed together with TAM-injected littermates. Therefore, non-induced Cre+ control mice were housed separately from TAM-injected cohorts.

**Stereotaxic intracerebral injection**

Intracerebral injection of DT from Corynebacterium diphtheriae (D0564; Sigma-Aldrich) into the cerebral cortex or thalamus was performed using stereotaxic alignment system (David Kopf Instruments). In brief, 6–8-wk-old *Sox10-Cre:iDTR Sun1-sfGFP* and control *Sox10-Cre:Sun1-sfGFP* mice were anesthetized with isoflurane and positioned in the stereotaxic frame. A 0.2 mm hole was drilled in the skull at coordinates of 1.0 mm posterior to bregma and 1.0 mm lateral to the midline in the right hemisphere. 1 ng of 1 ng/μl DT dissolved in artificial cerebrospinal fluid was injected at the depth of 1 mm below the surface of the skull for cortex and 3 mm for thalamus with a 33G needle attached to 5 μl Hamilton syringe. After 72 h, mice were transcardially perfused with ice cold PBS followed by ice cold 4% paraformaldehyde (PFA), and brains were isolated and processed for immunolabeling as described below.

**Neuroinflammation**

To induce neuroinflammation, 4–6-wk-old mice received a single i.p. injection of 4 mg/kg LPS from *Escherichia coli* O111:B4 (L4391; Sigma-Aldrich) or sterile saline 3 d after TAM induction. Mice were perfused 24 h or 5 d after injection, and brains were isolated and processed as described below.

**Immunolabeling and confocal imaging**

Immunolabeling was performed on cryosections as previously described (Chechneva et al., 2014; Mayrhofer et al., 2021). Mice were deeply anesthetized with isoflurane (5% for 6 min) and perfused with ice cold PBS followed by ice cold 4% PFA with flow rate 2 ml/min for 5 min each. Brains and spinal cords were dissected, postfixed in 4% PFA for 24 h and subsequently cryopreserved in 10 and 20% sucrose, embedded in OCT:20% sucrose 1:1 mixture in the vapor of liquid nitrogen. Tissues were cut in 15 μm sections on the cryostat. For immunolabeling, sections were washed 3 × 5 min with PBS to remove residues of OCT. Nonspecific binding of antibodies was blocked at room temperature (RT) for 30 min using 10% normal serum in 0.2% Triton-X in PBS. We used following antibodies: goat anti-mCherry (1:1,000; orb11618; Biorbyt), chicken anti-GFP (1:500;

NB100-1614; Novus Biologicals), rabbit anti-HA (1:50; 71-5500; Zymed), goat anti-Olig2 (1:200; AF2418; R&D), rabbit anti-Olig2 (1:200; AB109186; Abcam), rabbit anti-NeuN (1:500; ABN78; Millipore), mouse anti-NeuN (1:100; MAB377; Millipore), rat anti-NeuN (1:300; AB279297; Abcam), mouse anti-Cre recombinase (1:200, Clone 2D2, MAB3120; Millipore), rabbit anti-Iba1 (1:500; 019-19741; Wako), rat anti-GFAP (1:500, 345860; Millipore), rabbit anti-GABA (1:100; A2052; Sigma-Aldrich), mouse anti-vGlut2 (1:100; MAB5504; Millipore), rabbit anti-NG2 (1:200; AB5320; Millipore), goat anti-PDGFRα (1:500; AF1062; R&D Systems), rabbit anti-Sox10 (1:1,000; ab155279; Abcam), mouse anti-APC (clone CC1; 1:200; OP80; Calbiochem), rat anti-MBP (1:50; NB600-717; Novus Biologicals) diluted in PBS containing 5% normal serum, and 0.2% Triton-X. Sections were incubated either for 2 h at RT or overnight at 4°C. After 3 × 10 min wash with PBS, sections were incubated with fluorophore-conjugated secondary antibodies Alexa Fluor-405, 488, 594 or 647 (1:1,000; Life Technologies) to detect primary antibody. Slides were mounted using DAPI Fluoromount-G (SouthernBiotech). For staining containing Alexa Fluor 405, slides were mounted using Fluoromount-G without DAPI.

Images were acquired on Nikon Eclipse 90i A1 or Nikon Eclipse Ti2 C2 laser scanning confocal microscopes. Negative controls omitting primary antibody were performed to confirm specificity of staining. In constitutive *Sox10-Cre* mice, cells were counted in low magnification images (×20 objective) in right and left hemispheres of coronal sections in the cortex, thalamus, striatal caudate putamen, and hippocampal DG of four sections from three or more mice for each condition. In inducible *Sox10-iCreER[T2]* mice, cells were counted through the defined area of cortical layers 2–3 of four coronal sections per mouse. Cell numbers are presented per mm². Quantification was performed by an investigator blinded to the experimental groups. Mean fluorescence intensity was measured using ImageJ (NIH).

Images were processed using NIS-Elements Imaging Software, ImageJ, and Adobe Photoshop CC.

**Super-resolution microscopy**

Super-resolution imaging was performed using a Leica SP8 Falcon confocal microscope with a Lighting detector module. A Z-stack of 1,320 × 1,320 images was acquired. Processing of images with the Lighting detector module achieved a sub-diffraction limited resolution image of ∼120 nm. Images were processed using ImageJ (NIH). Movie was created from the Z-stack series using ImageJ.

**TEM**

Adult *Sox10-Cre:Rpl10a-EGFP* mice were deeply anesthetized with isoflurane (5% for 6 min) and perfused through the heart with 1 ml of 1,000 units heparin followed by ice cold mixture of 2% PFA and 2% glutaraldehyde in 0.1 M Sorensen's Buffer with flow rate 2 ml/min for 30 min. Brains were removed and postfixed in 3% glutaraldehyde. Brains were sectioned in 1-mm coronal sections using brain cutting block. 1 × 1 mm areas of somatosensory cortex layers 2–4 and thalamus were isolated under dissecting microscope. Tissue blocks were processed using previously described protocol (Wang et al., 2022) with

Mayrhofer et al.
Neurons receive material from Sox10-lineage cells

Journal of Experimental Medicine 11 of 15
https://doi.org/10.1084/jem.20221632

modifications. In brief, tissue blocks were washed twice for 10 min in 0.2 M sodium cacodylate buffer (Cat. #1160110; Electron Microscopy Sciences) at RT and postfixed in 2% osmium tetroxide (Cat. #19152; Electron Microscopy Sciences) in water for 1.5 h. All following washes were performed at RT on a rotator at 10 rpm. After washing 2 × 10 min in 0.2 M sodium cacodylate buffer followed by 2 × 5 min in distilled water, sections were dehydrated by washing 2 × 30 min in 50, 70, 90, and 100% ethanol followed by 2 × 30 min wash in propylene oxide. Tissue blocks were incubated in 1:1 mixture of propylene oxide and eponate resin (EMBed-812 cat. #14120; Electron Microscopy Sciences) overnight at RT. The next day, tissue blocks were incubated in 1:3 mixture of propylene oxide:eponate resin followed by incubation in pure eponate resin overnight. The next morning, tissue blocks were embedded in eponate resin by incubation at 60°C for 6 h. 80-nm ultrathin sections were cut on a Leica EM UC5 ultramicrotome and collected on Formvar carbon film-coated single-slot copper grids (Cat. #FCF2010-CU; Electron Microscopy Sciences). Sections were stained with 4% uranyl acetate followed by 3% lead citrate to enhance contrast. TEM images were obtained on FEI Talos L120C TEM equipped with CETA 16 MP camera at the Biological Electron Microscopy Facility at UC Davis.

### Fluorescence-activated nuclei sorting
Mice were euthanized using $CO_2$ and cortical and thalamic areas were isolated on ice, and flash-frozen in liquid nitrogen for further use. Brain tissue was homogenized in 2 ml of lysis buffer (10 mM Tris-HCl, pH 7.4, 10 mM NaCl, 3 mM $MgCl_2$, and 0.025% NP-40) in a Dounce homogenizer, and incubated on ice for 15 min. The suspension was filtered through a 30 µm filter to remove debris and pelleted at 500 ×$g$ for 5 min at 4°C. The pellet was washed with 1 ml of nuclei wash buffer (1% BSA in PBS) twice and passed through a 30 µm filter into a 2 ml tube. After centrifugation at 500 ×$g$ for 5 min, the pellet was resuspended in 450 µl nuclei wash buffer and 810 µl 1.8 M sucrose and carefully overlayed on top of 500 µl 1.8 M sucrose in a 2 ml tube. Gradient was centrifuged at 13,000 ×$g$ for 45 min at 4°C to separate nuclei from myelin debris. Supernatant was discarded until 100 µl bottom fraction containing the nuclei. Nuclei fraction was washed with 1 ml nuclei wash buffer and resuspended in 400 µl nuclei wash buffer filtered through a 40-µm FlowMi Cell Strainer. Nuclei were counted using hematocytometer and transferred to staining plates (12565502; Thermo Fisher Scientific). After washing with sorting buffer (PBS plus 1% BSA, 0.1% sodium azide, 2 mM EDTA), nuclei were stained with rabbit anti-NeuN Alexa-647 (1:200; 62994; Cell Signaling) and rat anti-GFP Alexa-488 (1:200; 338007; BioLegend) on ice for 30–60 min. Nuclei were washed, pelleted by centrifugation at 350 ×$g$ for 3 × 5 min at 4°C, and counterstained with DAPI for 5 min at 4°C. After washing, nuclei resuspended in sorting buffer were analyzed on Attune NxT Acoustic Focusing Cytometer (Life Technologies). Unstained nuclei, single-stain controls, fluorescence minus one, and stained AbC Total Antibody Compensation beads (A10497; Thermo Fisher Scientific) were used for each experiment to determine compensation parameters and gating. Acquired data were analyzed using FlowJo software (TreeStar).

Nuclei populations were gated for single events positive for DAPI, NeuN, and GFP. The data are presented as the percentage of NeuN+ nuclei population.

### Statistics
Statistical analysis was performed using GraphPad Prism 7.5. The number of animals per group used for each study is shown in the figures where each point represents an individual animal. P values were determined using unpaired $t$ test for two group comparison or one-way ANOVA with Bonferroni post hoc test to compare three and more groups. Correlation was computed using Pearson correlation analysis. In all figures, data are represented as mean ± SEM. In all cases, probability values <0.05 were considered statistically significant. Figures were assembled using Adobe Illustrator CC.

### Online supplemental material
Fig. S1 shows the distribution of ribosomal material in neurons throughout the CNS, Cre-negative control, gating strategy, and quantification for fluorescence-activated nuclei sorting and confocal analysis of astrocytes and microglia in *Sox10-Cre:Rpl10a-EGFP* mice (related to Fig. 1). Fig. S2 shows accumulation of ribosomal Rpl10a-EGFP reporter in neurons in *PDGFRα-Cre:Rpl10a-EGFP* mice in comparison with control *PDGFRα-Cre:EYFP* mice and abnormal craniofacial phenotype in *Sox10-Cre:Rpl10a-EGFP* and *Sox10-Cre:Rpl10a-EGFP H2B-mCherry* mice (related to Fig. 1). Fig. S3 shows the presence of reporter-positive neurons in different brain regions in nuclear reporter *Sox10-iCreER^T2:Sun1-sfGFP* mice after TAM induction, response of material transfer to LPS in *Sox10-iCreER^T2:Rpl10a-EGFP* mice, SOL-neuron nuclear pairs in *Sox10-Cre:Rpl10a-EGFP H2B-mCherry* mice and TEM of satellite SOL-neuron pair separated by plasma membrane (related to Figs. 4 and 5). Video 1 shows Z-stack through Sun1-sfGFP+ satellite SOL-neuron nuclear pair in the cortex of *Sox10-iCreER^T2:Sun1-sfGFP* mice obtained by super-resolution confocal imaging (related to Fig. 5).

### Data availability
All transgenic mice used in this study were obtained from the Jackson Laboratory. All data underlying the conclusions are presented in the paper and its supplemental material.

## References

Achilleos, A., and P.A. Trainor. 2015. Mouse models of rare craniofacial disorders. *Curr. Top. Dev. Biol.* 115:413–458. https://doi.org/10.1016/bs.ctdb.2015.07.011

Alvarez-Dolado, M., R. Pardal, J.M. Garcia-Verdugo, J.R. Fike, H.O. Lee, K. Pfeffer, C. Lois, S.J. Morrison, and A. Alvarez-Buylla. 2003. Fusion of bone-marrow-derived cells with Purkinje neurons, cardiomyocytes and hepatocytes. *Nature*. 425:968–973. https://doi.org/10.1038/nature02069

Antón-Bolaños, N., A. Espinosa, and G. López-Bendito. 2018. Developmental interactions between thalamus and cortex: A true love reciprocal story. *Curr. Opin. Neurobiol.* 52:33–41. https://doi.org/10.1016/j.conb.2018.04.018

Asai, H., S. Ikezu, S. Tsunoda, M. Medalla, J. Luebke, T. Haydar, B. Wolozin, O. Butovsky, S. Kügler, and T. Ikezu. 2015. Depletion of microglia and inhibition of exosome synthesis halt tau propagation. *Nat. Neurosci.* 18:1584–1593. https://doi.org/10.1038/nn.4132

Attwell, D., and S.B. Laughlin. 2001. An energy budget for signaling in the grey matter of the brain. *J. Cereb. Blood Flow Metab.* 21:1133–1145. https://doi.org/10.1097/00004647-200110000-00001

Barateiro, A., and A. Fernandes. 2014. Temporal oligodendrocyte lineage progression: In vitro models of proliferation, differentiation and myelination. *Biochim. Biophys. Acta*. 1843:1917–1929. https://doi.org/10.1016/j.bbamcr.2014.04.018

Batista, C.R.A., G.F. Gomes, E. Candelario-Jalil, B.L. Fiebich, and A.C.P. de Oliveira. 2019. Lipopolysaccharide-induced neuroinflammation as a bridge to understand neurodegeneration. *Int. J. Mol. Sci.* 20:20. https://doi.org/10.3390/ijms20092293

Battefeld, A., J. Klooster, and M.H. Kole. 2016. Myelinating satellite oligodendrocytes are integrated in a glial syncytium constraining neuronal high-frequency activity. *Nat. Commun.* 7:11298. https://doi.org/10.1038/ncomms11298

Bowles, J., G. Schepers, and P. Koopman. 2000. Phylogeny of the SOX family of developmental transcription factors based on sequence and structural indicators. *Dev. Biol.* 227:239–255. https://doi.org/10.1006/dbio.2000.9883

Bronner, M.E., and M. Simões-Costa. 2016. The neural crest migrating into the twenty-first century. *Curr. Top. Dev. Biol.* 116:115–134. https://doi.org/10.1016/bs.ctdb.2015.12.003

Brown, G.C. 2019. The endotoxin hypothesis of neurodegeneration. *J. Neuroinflammation*. 16:180. https://doi.org/10.1186/s12974-019-1564-7

Buch, T., F.L. Heppner, C. Tertilt, T.J. Heinen, M. Kremer, F.T. Wunderlich, S. Jung, and A. Waisman. 2005. A Cre-inducible diphtheria toxin receptor mediates cell lineage ablation after toxin administration. *Nat. Methods*. 2:419–426. https://doi.org/10.1038/nmeth762

Buchwalter, A., R. Schulte, H. Tsai, J. Capitanio, and M. Hetzer. 2019. Selective clearance of the inner nuclear membrane protein emerin by vesicular transport during ER stress. *Elife*. 8:e49796. https://doi.org/10.7554/eLife.49796

Chamberlain, K.A., N. Huang, Y. Xie, F. LiCausi, S. Li, Y. Li, and Z.H. Sheng. 2021. Oligodendrocytes enhance axonal energy metabolism by deacetylation of mitochondrial proteins through transcellular delivery of SIRT2. *Neuron*. 109:3456–3472. https://doi.org/10.1016/j.neuron.2021.08.011

Chechneva, O.V., F. Mayrhofer, D.J. Daugherty, R.G. Krishnamurty, P. Bannerman, D.E. Pleasure, and W. Deng. 2014. A Smoothened receptor agonist is neuroprotective and promotes regeneration after ischemic brain injury. *Cell Death Dis.* 5:e1481. https://doi.org/10.1038/cddis.2014.446

Court, F.A., W.T. Hendriks, H.D. MacGillavry, J. Alvarez, and J. van Minnen. 2008. Schwann cell to axon transfer of ribosomes: Toward a novel understanding of the role of glia in the nervous system. *J. Neurosci.* 28:11024–11029. https://doi.org/10.1523/JNEUROSCI.2429-08.2008

Damisah, E.C., R.A. Hill, A. Rai, F. Chen, C.V. Rothlin, S. Ghosh, and J. Grutzendler. 2020. Astrocytes and microglia play orchestrated roles and respect phagocytic territories during neuronal corpse removal in vivo. *Sci. Adv.* 6:eaba3239. https://doi.org/10.1126/sciadv.aba3239

Đặng, T.C., Y. Ishii, V. Nguyen, S. Yamamoto, T. Hamashima, N. Okuno, Q.L. Nguyen, Y. Sang, N. Ohkawa, Y. Saitoh, et al. 2019. Powerful homeostatic control of oligodendroglial lineage by PDGFRα in adult brain. *Cell Rep.* 27:1073–1089.e5. https://doi.org/10.1016/j.celrep.2019.03.084

Denk, F., L.M. Ramer, E.L. Erskine, M.A. Nassar, Y. Bogdanov, J.N. Wood, S.B. McMahon, and M.S. Ramer. 2015. Tamoxifen induces cellular stress in the nervous system by inhibiting cholesterol synthesis. *Acta Neuropathol. Commun.* 3:74. https://doi.org/10.1186/s40478-015-0255-6

DiFiglia, M., E. Sapp, K.O. Chase, S.W. Davies, G.P. Bates, J.P. Vonsattel, and N. Aronin. 1997. Aggregation of huntingtin in neuronal intranuclear inclusions and dystrophic neurites in brain. *Science*. 277:1990–1993. https://doi.org/10.1126/science.277.5334.1990

Dörrbaum, A.R., L. Kochen, J.D. Langer, and E.M. Schuman. 2018. Local and global influences on protein turnover in neurons and glia. *Elife*. 7:e34202. https://doi.org/10.7554/eLife.34202

Downes, N., and P. Mullins. 2014. The development of myelin in the brain of the juvenile rat. *Toxicol. Pathol.* 42:913–922. https://doi.org/10.1177/0192623313503518

Farley-Barnes, K.I., L.M. Ogawa, and S.J. Baserga. 2019. Ribosomopathies: Old concepts, new controversies. *Trends Genet.* 35:754–767. https://doi.org/10.1016/j.tig.2019.07.004

Foran, D.R., and A.C. Peterson. 1992. Myelin acquisition in the central nervous system of the mouse revealed by an MBP-Lac Z transgene. *J. Neurosci.* 12:4890–4897. https://doi.org/10.1523/JNEUROSCI.12-12-04890.1992

Frühbeis, C., D. Fröhlich, W.P. Kuo, J. Amphornrat, S. Thilemann, A.S. Saab, F. Kirchhoff, W. Möbius, S. Goebbels, K.A. Nave, et al. 2013. Neurotransmitter-triggered transfer of exosomes mediates oligodendrocyte-neuron communication. *PLoS Biol.* 11:e1001604. https://doi.org/10.1371/journal.pbio.1001604

Frühbeis, C., W.P. Kuo-Elsner, C. Müller, K. Barth, L. Peris, S. Tenzer, W. Möbius, H.B. Werner, K.A. Nave, D. Fröhlich, and E.M. Krämer-Albers. 2020. Oligodendrocytes support axonal transport and maintenance via exosome secretion. *PLoS Biol.* 18:e3000621. https://doi.org/10.1371/journal.pbio.3000621

Glenner, G.G., and C.W. Wong. 1984. Alzheimer's disease: Initial report of the purification and characterization of a novel cerebrovascular amyloid protein. *Biochem. Biophys. Res. Commun.* 120:885–890. https://doi.org/10.1016/S0006-291X(84)80190-4

Götz, M., and W.B. Huttner. 2005. The cell biology of neurogenesis. *Nat. Rev. Mol. Cell Biol.* 6:777–788. https://doi.org/10.1038/nrm1739

Guo, M., J. Wang, Y. Zhao, Y. Feng, S. Han, Q. Dong, M. Cui, and K. Tieu. 2020. Microglial exosomes facilitate α-synuclein transmission in Parkinson's disease. *Brain*. 143:1476–1497. https://doi.org/10.1093/brain/awaa090

Harris, J.J., and D. Attwell. 2012. The energetics of CNS white matter. *J. Neurosci.* 32:356–371. https://doi.org/10.1523/JNEUROSCI.3430-11.2012

Hasel, P., I.V.L. Rose, J.S. Sadick, R.D. Kim, and S.A. Liddelow. 2021. Neuroinflammatory astrocyte subtypes in the mouse brain. *Nat. Neurosci.* 24:1475–1487. https://doi.org/10.1038/s41593-021-00905-6

Heppner, F.L., R.M. Ransohoff, and B. Becher. 2015. Immune attack: The role of inflammation in Alzheimer disease. *Nat. Rev. Neurosci.* 16:358–372. https://doi.org/10.1038/nrn3880

Hill, R.A., K.D. Patel, C.M. Goncalves, J. Grutzendler, and A. Nishiyama. 2014. Modulation of oligodendrocyte generation during a critical temporal window after NG2 cell division. *Nat. Neurosci.* 17:1518–1527. https://doi.org/10.1038/nn.3815

Hoogland, I.C., C. Houbolt, D.J. van Westerloo, W.A. van Gool, and D. van de Beek. 2015. Systemic inflammation and microglial activation: Systematic review of animal experiments. *J. Neuroinflammation*. 12:114. https://doi.org/10.1186/s12974-015-0332-6

Hughes, E.G., S.H. Kang, M. Fukaya, and D.E. Bergles. 2013. Oligodendrocyte progenitors balance growth with self-repulsion to achieve homeostasis

in the adult brain. *Nat. Neurosci.* 16:668–676. https://doi.org/10.1038/nn.3390

Jernigan, T.L., W.F. Baaré, J. Stiles, and K.S. Madsen. 2011. Postnatal brain development: Structural imaging of dynamic neurodevelopmental processes. *Prog. Brain Res.* 189:77–92. https://doi.org/10.1016/B978-0-444-53884-0.00019-1

Jonas, R.A., T.F. Yuan, Y.X. Liang, J.B. Jonas, D.K. Tay, and R.G. Ellis-Behnke. 2012. The spider effect: Morphological and orienting classification of microglia in response to stimuli in vivo. *PLoS One.* 7:e30763. https://doi.org/10.1371/journal.pone.0030763

Kalargyrou, A.A., M. Basche, A. Hare, E.L. West, A.J. Smith, R.R. Ali, and R.A. Pearson. 2021. Nanotube-like processes facilitate material transfer between photoreceptors. *EMBO Rep.* 22:e53732. https://doi.org/10.15252/embr.202153732

Kealy, J., C. Murray, E.W. Griffin, A.B. Lopez-Rodriguez, D. Healy, L.S. Tortorelli, J.P. Lowry, L.O. Watne, and C. Cunningham. 2020. Acute inflammation alters brain energy metabolism in mice and humans: Role in suppressed spontaneous activity, impaired cognition, and delirium. *J. Neurosci.* 40:5681–5696. https://doi.org/10.1523/JNEUROSCI.2876-19.2020

Kloss, C.U., M. Bohatschek, G.W. Kreutzberg, and G. Raivich. 2001. Effect of lipopolysaccharide on the morphology and integrin immunoreactivity of ramified microglia in the mouse brain and in cell culture. *Exp. Neurol.* 168:32–46. https://doi.org/10.1006/exnr.2000.7575

Kosik, K.S., C.L. Joachim, and D.J. Selkoe. 1986. Microtubule-associated protein tau (tau) is a major antigenic component of paired helical filaments in Alzheimer disease. *Proc. Natl. Acad. Sci. USA.* 83:4044–4048. https://doi.org/10.1073/pnas.83.11.4044

Kougioumtzidou, E., T. Shimizu, N.B. Hamilton, K. Tohyama, R. Sprengel, H. Monyer, D. Attwell, and W.D. Richardson. 2017. Signalling through AMPA receptors on oligodendrocyte precursors promotes myelination by enhancing oligodendrocyte survival. *Elife.* 6:e28080. https://doi.org/10.7554/eLife.28080

Kroon, T., E. van Hugte, L. van Linge, H.D. Mansvelder, and R.M. Meredith. 2019. Early postnatal development of pyramidal neurons across layers of the mouse medial prefrontal cortex. *Sci. Rep.* 9:5037. https://doi.org/10.1038/s41598-019-41661-9

Kruger, L., and D.S. Maxwell. 1966. Electron microscopy of oligodendrocytes in normal rat cerebrum. *Am. J. Anat.* 118:411–435. https://doi.org/10.1002/aja.1001180207

Kuhlbrodt, K., B. Herbarth, E. Sock, I. Hermans-Borgmeyer, and M. Wegner. 1998. Sox10, a novel transcriptional modulator in glial cells. *J. Neurosci.* 18:237–250. https://doi.org/10.1523/JNEUROSCI.18-01-00237.1998

Küspert, M., A. Hammer, M.R. Bösl, and M. Wegner. 2011. Olig2 regulates Sox10 expression in oligodendrocyte precursors through an evolutionary conserved distal enhancer. *Nucleic Acids Res.* 39:1280–1293. https://doi.org/10.1093/nar/gkq951

Liddelow, S.A., K.A. Guttenplan, L.E. Clarke, F.C. Bennett, C.J. Bohlen, L. Schirmer, M.L. Bennett, A.E. Münch, W.S. Chung, T.C. Peterson, et al. 2017. Neurotoxic reactive astrocytes are induced by activated microglia. *Nature.* 541:481–487. https://doi.org/10.1038/nature21029

Ling, J.P., O. Pletnikova, J.C. Troncoso, and P.C. Wong. 2015. TDP-43 repression of nonconserved cryptic exons is compromised in ALS-FTD. *Science.* 349:650–655. https://doi.org/10.1126/science.aab0983

Liu, J., A.M. Krautzberger, S.H. Sui, O.M. Hofmann, Y. Chen, M. Baetscher, I. Grgic, S. Kumar, B.D. Humphreys, W.A. Hide, and A.P. McMahon. 2014. Cell-specific translational profiling in acute kidney injury. *J. Clin. Invest.* 124:1242–1254. https://doi.org/10.1172/JCI72126

López-Bendito, G., and Z. Molnár. 2003. Thalamocortical development: How are we going to get there? *Nat. Rev. Neurosci.* 4:276–289. https://doi.org/10.1038/nrn1075

Lopez-Verrilli, M.A., F. Picou, and F.A. Court. 2013. Schwann cell-derived exosomes enhance axonal regeneration in the peripheral nervous system. *Glia.* 61:1795–1806. https://doi.org/10.1002/glia.22558

Luarte, A., R. Henzi, A. Fernández, D. Gaete, P. Cisternas, M. Pizarro, L.F. Batiz, I. Villalobos, M. Masalleras, R. Vergara, et al. 2020. Astrocyte-derived small extracellular vesicles regulate dendritic complexity through miR-26a-5p activity. *Cells.* 9:930. https://doi.org/10.3390/cells9040930

Martínez-Cerdeño, V., B.L. Barrilleaux, A. McDonough, J. Ariza, B.T.K. Yuen, P. Somanath, C.T. Le, C. Steward, K. Horton-Sparks, and P.S. Knoepfler. 2017. Behavior of xeno-transplanted undifferentiated human induced pluripotent stem cells is impacted by microenvironment without evidence of tumors. *Stem Cells Dev.* 26:1409–1423. https://doi.org/10.1089/scd.2017.0059

Mayrhofer, F., Z. Dariychuk, A. Zhen, D.J. Daugherty, P. Bannerman, A.M. Hanson, D. Pleasure, A. Soulika, W. Deng, and O.V. Chechneva. 2021. Reduction in CD11c+ microglia correlates with clinical progression in chronic experimental autoimmune demyelination. *Neurobiol. Dis.* 161:105556. https://doi.org/10.1016/j.nbd.2021.105556

McKenzie, I.A., D. Ohayon, H. Li, J.P. de Faria, B. Emery, K. Tohyama, and W.D. Richardson. 2014. Motor skill learning requires active central myelination. *Science.* 346:318–322. https://doi.org/10.1126/science.1254960

Mittli, D., V. Tukacs, L. Ravasz, É. Csősz, T. Kozma, J. Kardos, G. Juhász, and K.A. Kékesi. 2023. LPS-induced acute neuroinflammation, involving interleukin-1 beta signaling, leads to proteomic, cellular, and network-level changes in the prefrontal cortex of mice. *Brain Behav. Immun. Health.* 28:100594. https://doi.org/10.1016/j.bbih.2023.100594

Mizuno, H., K. Ikezoe, S. Nakazawa, T. Sato, K. Kitamura, and T. Iwasato. 2018. Patchwork-type spontaneous activity in neonatal barrel cortex layer 4 transmitted via thalamocortical projections. *Cell Rep.* 22:123–135. https://doi.org/10.1016/j.celrep.2017.12.012

Mo, A., E.A. Mukamel, F.P. Davis, C. Luo, G.L. Henry, S. Picard, M.A. Urich, J.R. Nery, T.J. Sejnowski, R. Lister, et al. 2015. Epigenomic signatures of neuronal diversity in the mammalian brain. *Neuron.* 86:1369–1384. https://doi.org/10.1016/j.neuron.2015.05.018

Morrison, B.M., Y. Lee, and J.D. Rothstein. 2013. Oligodendroglia: Metabolic supporters of axons. *Trends Cell Biol.* 23:644–651. https://doi.org/10.1016/j.tcb.2013.07.007

Müller, K., A. Schnatz, M. Schillner, S. Woertge, C. Müller, I. von Graevenitz, A. Waisman, J. van Minnen, and C.F. Vogelaar. 2018. A predominantly glial origin of axonal ribosomes after nerve injury. *Glia.* 66:1591–1610. https://doi.org/10.1002/glia.23327

Nahirney, P.C., and M.E. Tremblay. 2021. Brain ultrastructure: Putting the pieces together. *Front. Cell Dev. Biol.* 9:629503. https://doi.org/10.3389/fcell.2021.629503

Neumann, M., D.M. Sampathu, L.K. Kwong, A.C. Truax, M.C. Micsenyi, T.T. Chou, J. Bruce, T. Schuck, M. Grossman, C.M. Clark, et al. 2006. Ubiquitinated TDP-43 in frontotemporal lobar degeneration and amyotrophic lateral sclerosis. *Science.* 314:130–133. https://doi.org/10.1126/science.1134108

Ortin-Martinez, A., N.E. Yan, E.L.S. Tsai, L. Comanita, A. Gurdita, Z.C. Liu, S. Lu, P. Dolati, N.T. Pokrajac, et al. 2021. Photoreceptor nanotubes mediate the in vivo exchange of intracellular material. *EMBO J.* 40:e107264. https://doi.org/10.15252/embj.2020107264

Paolicelli, R.C., G. Bolasco, F. Pagani, L. Maggi, M. Scianni, P. Panzanelli, M. Giustetto, T.A. Ferreira, E. Guiducci, L. Dumas, et al. 2011. Synaptic pruning by microglia is necessary for normal brain development. *Science.* 333:1456–1458. https://doi.org/10.1126/science.1202529

Patel, M.R., and A.M. Weaver. 2021. Astrocyte-derived small extracellular vesicles promote synapse formation via fibulin-2-mediated TGF-β signaling. *Cell Rep.* 34:108829. https://doi.org/10.1016/j.celrep.2021.108829

Pearson, R.A., A. Gonzalez-Cordero, E.L. West, J.R. Ribeiro, N. Aghaizu, D. Goh, R.D. Sampson, A. Georgiadis, P.V. Waldron, Y. Duran, et al. 2016. Donor and host photoreceptors engage in material transfer following transplantation of post-mitotic photoreceptor precursors. *Nat. Commun.* 7:13029. https://doi.org/10.1038/ncomms13029

Peron, S.P., J. Freeman, V. Iyer, C. Guo, and K. Svoboda. 2015. A cellular resolution map of barrel cortex activity during tactile behavior. *Neuron.* 86:783–799. https://doi.org/10.1016/j.neuron.2015.03.027

Philips, T., Y.A. Mironova, Y. Jouroukhin, J. Chew, S. Vidensky, M.H. Farah, M.V. Pletnikov, D.E. Bergles, B.M. Morrison, and J.D. Rothstein. 2021. MCT1 deletion in oligodendrocyte lineage cells causes late-onset hypomyelination and axonal degeneration. *Cell Rep.* 34:108610. https://doi.org/10.1016/j.celrep.2020.108610

Rakic, P. 2009. Evolution of the neocortex: A perspective from developmental biology. *Nat. Rev. Neurosci.* 10:724–735. https://doi.org/10.1038/nrn2719

Rice, D., and S. Barone Jr. 2000. Critical periods of vulnerability for the developing nervous system: Evidence from humans and animal models. *Environ. Health Perspect.* 108:511–533. https://doi.org/10.1289/ehp.00108s3511

Rivers, L.E., K.M. Young, M. Rizzi, F. Jamen, K. Psachoulia, A. Wade, N. Kessaris, and W.D. Richardson. 2008. PDGFRA/NG2 glia generate myelinating oligodendrocytes and piriform projection neurons in adult mice. *Nat. Neurosci.* 11:1392–1401. https://doi.org/10.1038/nn.2220

Roh, H.C., L.T. Tsai, A. Lyubetskaya, D. Tenen, M. Kumari, and E.D. Rosen. 2017. Simultaneous transcriptional and epigenomic profiling from specific cell types within heterogeneous tissues in vivo. *Cell Rep.* 18:1048–1061. https://doi.org/10.1016/j.celrep.2016.12.087

Rostami, J., S. Holmqvist, V. Lindström, J. Sigvardson, G.T. Westermark, M. Ingelsson, J. Bergström, L. Roybon, and A. Erlandsson. 2017. Human astrocytes transfer aggregated alpha-synuclein via tunneling nanotubes. *J. Neurosci.* 37: 11835–11853. https://doi.org/10.1523/JNEUROSCI.0983-17.2017

Sanz, E., L. Yang, T. Su, D.R. Morris, G.S. McKnight, and P.S. Amieux. 2009. Cell-type-specific isolation of ribosome-associated mRNA from complex tissues. *Proc. Natl. Acad. Sci. USA.* 106:13939–13944. https://doi.org/10.1073/pnas.0907143106

Semple, B.D., K. Blomgren, K. Gimlin, D.M. Ferriero, and L.J. Noble-Haeusslein. 2013. Brain development in rodents and humans: Identifying benchmarks of maturation and vulnerability to injury across species. *Prog. Neurobiol.* 106–107:1–16. https://doi.org/10.1016/j.pneurobio.2013.04.001

Shakhbazau, A., G.J. Schenk, C. Hay, J. Kawasoe, R. Klaver, V.W. Yong, J.J. Geurts, and J. van Minnen. 2016. Demyelination induces transport of ribosome-containing vesicles from glia to axons: Evidence from animal models and MS patient brains. *Mol. Biol. Rep.* 43:495–507. https://doi.org/10.1007/s11033-016-3990-2

Shi, Z., K. Fujii, K.M. Kovary, N.R. Genuth, H.L. Röst, M.N. Teruel, and M. Barna. 2017. Heterogeneous ribosomes preferentially translate distinct subpools of mRNAs genome-wide. *Mol. Cell.* 67:71–83.e7. https://doi.org/10.1016/j.molcel.2017.05.021

Shulman, R.G., D.L. Rothman, K.L. Behar, and F. Hyder. 2004. Energetic basis of brain activity: Implications for neuroimaging. *Trends Neurosci.* 27: 489–495. https://doi.org/10.1016/j.tins.2004.06.005

Spillantini, M.G., R.A. Crowther, R. Jakes, M. Hasegawa, and M. Goedert. 1998. alpha-Synuclein in filamentous inclusions of Lewy bodies from Parkinson's disease and dementia with lewy bodies. *Proc. Natl. Acad. Sci. USA.* 95:6469–6473. https://doi.org/10.1073/pnas.95.11.6469

Srinivas, S., T. Watanabe, C.S. Lin, C.M. William, Y. Tanabe, T.M. Jessell, and F. Costantini. 2001. Cre reporter strains produced by targeted insertion of EYFP and ECFP into the ROSA26 locus. *BMC Dev. Biol.* 1:4. https://doi.org/10.1186/1471-213X-1-4

Stolt, C.C., S. Rehberg, M. Ader, P. Lommes, D. Riethmacher, M. Schachner, U. Bartsch, and M. Wegner. 2002. Terminal differentiation of myelin-forming oligodendrocytes depends on the transcription factor Sox10. *Genes Dev.* 16:165–170. https://doi.org/10.1101/gad.215802

Takasaki, C., M. Yamasaki, M. Uchigashima, K. Konno, Y. Yanagawa, and M. Watanabe. 2010. Cytochemical and cytological properties of perineuronal oligodendrocytes in the mouse cortex. *Eur. J. Neurosci.* 32:1326–1336. https://doi.org/10.1111/j.1460-9568.2010.07377.x

Taniike, M., I. Mohri, N. Eguchi, C.T. Beuckmann, K. Suzuki, and Y. Urade. 2002. Perineuronal oligodendrocytes protect against neuronal apoptosis through the production of lipocalin-type prostaglandin D synthase in a genetic demyelinating model. *J. Neurosci.* 22:4885–4896. https://doi.org/10.1523/JNEUROSCI.22-12-04885.2002

Thomas, E.V., W.A. Fenton, J. McGrath, and A.L. Horwich. 2017. Transfer of pathogenic and nonpathogenic cytosolic proteins between spinal cord motor neurons in vivo in chimeric mice. *Proc. Natl. Acad. Sci. USA.* 114: E3139–E3148. https://doi.org/10.1073/pnas.1701465114

Wang, Y., B. Sun, B. Shibata, and F. Guo. 2022. Transmission electron microscopic analysis of myelination in the murine central nervous system. *STAR Protoc.* 3:101304. https://doi.org/10.1016/j.xpro.2022.101304

Weimann, J.M., C.A. Charlton, T.R. Brazelton, R.C. Hackman, and H.M. Blau. 2003a. Contribution of transplanted bone marrow cells to Purkinje neurons in human adult brains. *Proc. Natl. Acad. Sci. USA.* 100:2088–2093. https://doi.org/10.1073/pnas.0337659100

Weimann, J.M., C.B. Johansson, A. Trejo, and H.M. Blau. 2003b. Stable reprogrammed heterokaryons form spontaneously in Purkinje neurons after bone marrow transplant. *Nat. Cell Biol.* 5:959–966. https://doi.org/10.1038/ncb1053

Zamanian, J.L., L. Xu, L.C. Foo, N. Nouri, L. Zhou, R.G. Giffard, and B.A. Barres. 2012. Genomic analysis of reactive astrogliosis. *J. Neurosci.* 32: 6391–6410. https://doi.org/10.1523/JNEUROSCI.6221-11.2012

Zhan, X., B. Stamova, L.W. Jin, C. DeCarli, B. Phinney, and F.R. Sharp. 2016. Gram-negative bacterial molecules associate with Alzheimer disease pathology. *Neurology.* 87:2324–2332. https://doi.org/10.1212/WNL.0000000000003391

Zhang, R., R.G. Miller, R. Gascon, S. Champion, J. Katz, M. Lancero, A. Narvaez, R. Honrada, D. Ruvalcaba, and M.S. McGrath. 2009. Circulating endotoxin and systemic immune activation in sporadic amyotrophic lateral sclerosis (sALS). *J. Neuroimmunol.* 206:121–124. https://doi.org/10.1016/j.jneuroim.2008.09.017

Zhang, S., B. Kim, X. Zhu, X. Gui, Y. Wang, Z. Lan, P. Prabhu, K. Fond, A. Wang, and F. Guo. 2020. Glial type specific regulation of CNS angiogenesis by HIFα-activated different signaling pathways. *Nat. Commun.* 11:2027. https://doi.org/10.1038/s41467-020-15656-4
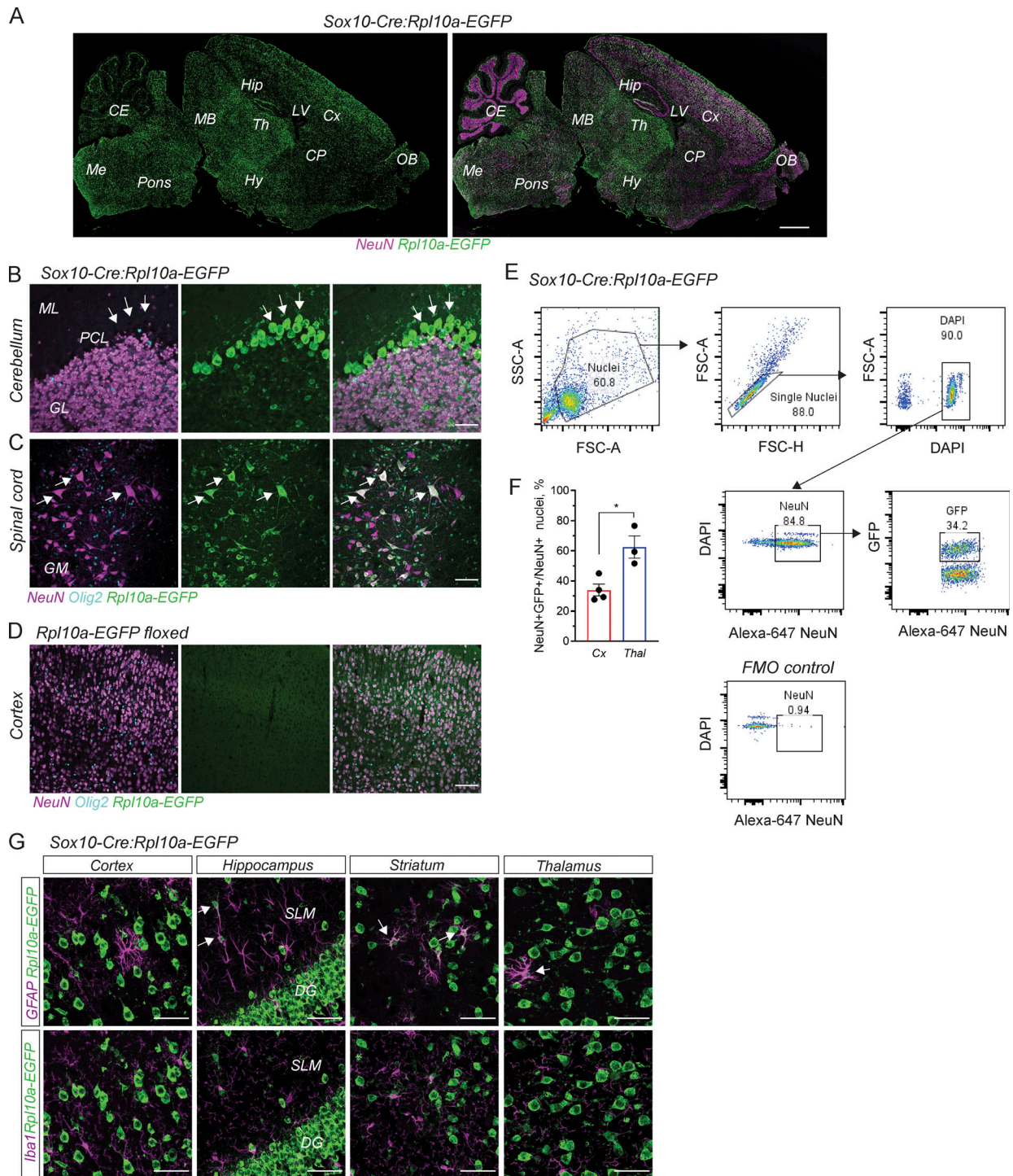
# Supplemental material

Figure S1. **SOL-derived ribosomal material accumulates in neurons throughout the entire CNS. (A)** Sagittal view showing distribution of reporter-positive neurons in the brain of adult *Sox10-Cre:Rpl10a-EGFP* mice. **(B)** Reporter-positive Purkinje neurons (arrows) were found in the cerebellum, while most of NeuN⁻ neurons in the molecular layer (ML) and NeuN⁺ neurons in the granular layer (GL) of the cerebellum were reporter-negative. **(C)** Reporter-positive pyramidal neurons (arrows) in the gray matter of the spinal cord in adult *Sox10-Cre:Rpl10a-EGFP* mice. **(D)** No Rpl10a-EGFP immunoreactivity was detected in the CNS of Cre-negative siblings carrying the *Rpl10a-EGFP* transgene. **(E)** Fluorescence-activated nuclei sorting analysis of NeuN⁺GFP⁺ nuclei isolated from the cortex or thalamus of adult *Sox10-Cre:Rpl10a-EGFP* mice. Gating for NeuN⁺ population was defined using fluorescence minus one (FMO) control. **(F)** Quantification of NeuN⁺GFP⁺ nuclei isolated from the cortex or thalamus. **(G)** No reporter-positive astrocytes (GFAP⁺) or microglia (Iba1⁺) were detected in the cortex of *Sox10-Cre:Rpl10a-EGFP* mice. Some reporter-positive astrocytes (arrows) were found in the hippocampal stratum lacunosum-moleculare (SLM), striatum and thalamus. No reporter-positive microglia were found in the hippocampus, striatum or thalamus. All data are presented as mean ± SEM. Each circle represents an individual animal. Data are representative of two (G) and three (A–F) independent experiments. P value was determined by unpaired *t* test. *, P < 0.05. Scale bars: 1,000 μm for A; 100 μm for C and D; 50 μm for B and G. CE, cerebellum; CP, caudate putamen, Cx, cortex; Hip, hippocampus; Hy, hypothalamus; LV, lateral ventricle; MB, midbrain; Me, medulla; OB, olfactory bulb; PCL, Purkinje cell layer; Th, thalamus.
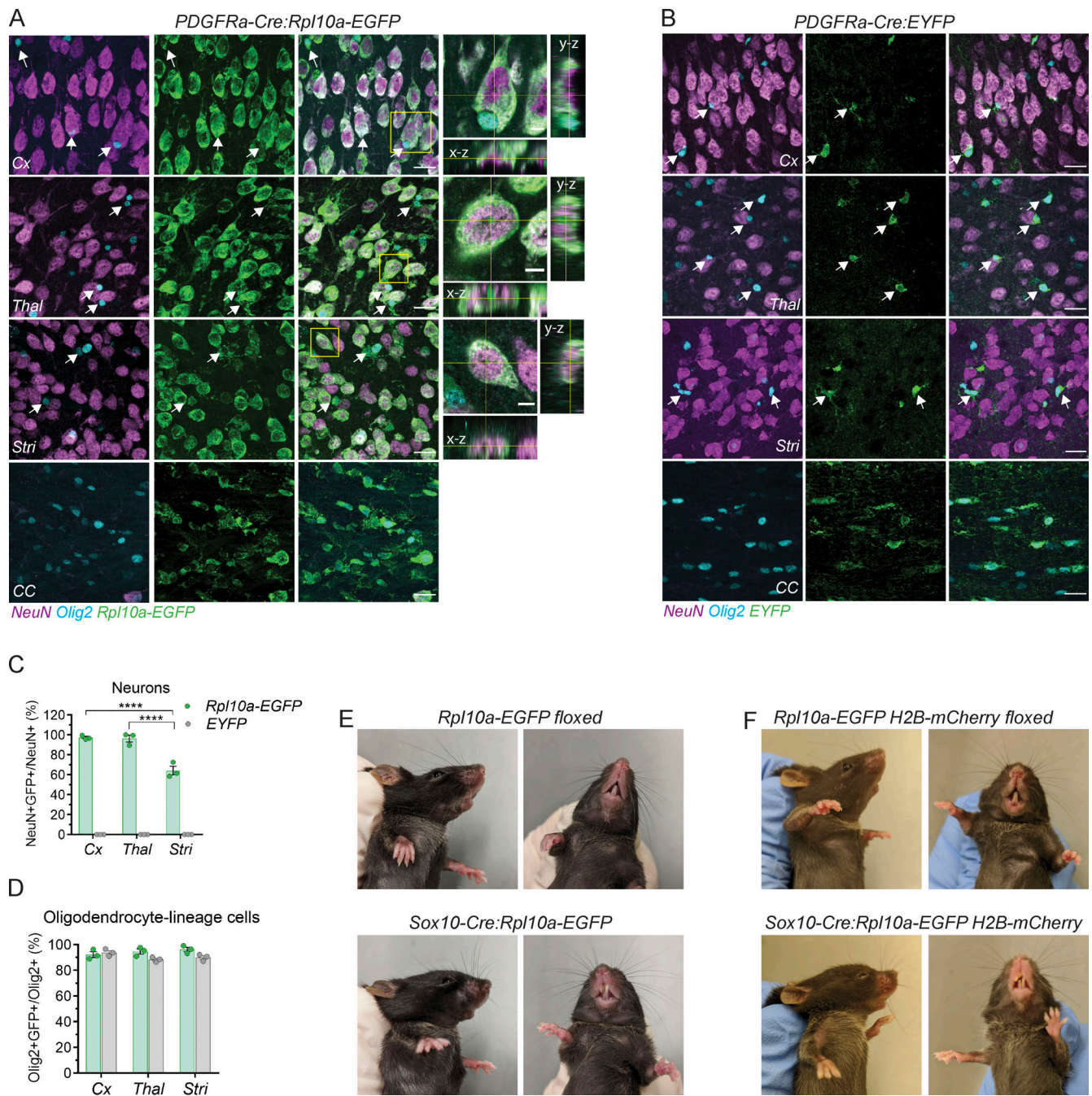
Figure S2. **Accumulation of oligodendrocyte-lineage cell-derived ribosomal reporter Rpl10a-EGFP in neurons. (A)** Ribosomal Rpl10a-EGFP reporter in oligodendrocyte-lineage cells (arrows) and neurons in the cortex, thalamus, striatum, and corpus callosum of adult *PDGFRα-Cre:Rpl10a-EGFP* mice. The region of the yellow box is enlarged and shown as a single plane image with orthogonal projection. **(B)** In adult *PDGFRα-Cre:EYFP* mice EYFP reporter protein was found only in oligodendrocyte-lineage cells (arrows) and not in neurons. **(C and D)** Quantification of reporter-positive NeuN+ neurons and Olig2+ oligodendrocyte-lineage cells in the cortex, thalamus, and striatum of adult *PDGFRα-Cre:Rpl10a-EGFP* and *PDGFRα-Cre:EYFP* mice. **(E and F)** *Sox10-Cre* mice carrying the *Rpl10a-EGFP* or *Rpl10a-EGFP H2B-mCherry* reporter allele had a distinct craniofacial phenotype, displaying malocclusion and runty appearance compared to Cre-negative siblings carrying the reporter allele. All data are presented as mean ± SEM. Each circle represents an individual animal. Data are representative of two (A–D) and four (E and F) independent experiments. P values were determined by two-way ANOVA with Bonferroni post hoc test. ****, $P < 0.0001$. Scale bars: 20 µm for A and B; 5 µm for enlargements in A. CC, corpus callosum; Cx, cortex; Stri, striatum; Thal, thalamus.

Mayrhofer et al.
Neurons receive material from Sox10-lineage cells

Journal of Experimental Medicine   S3
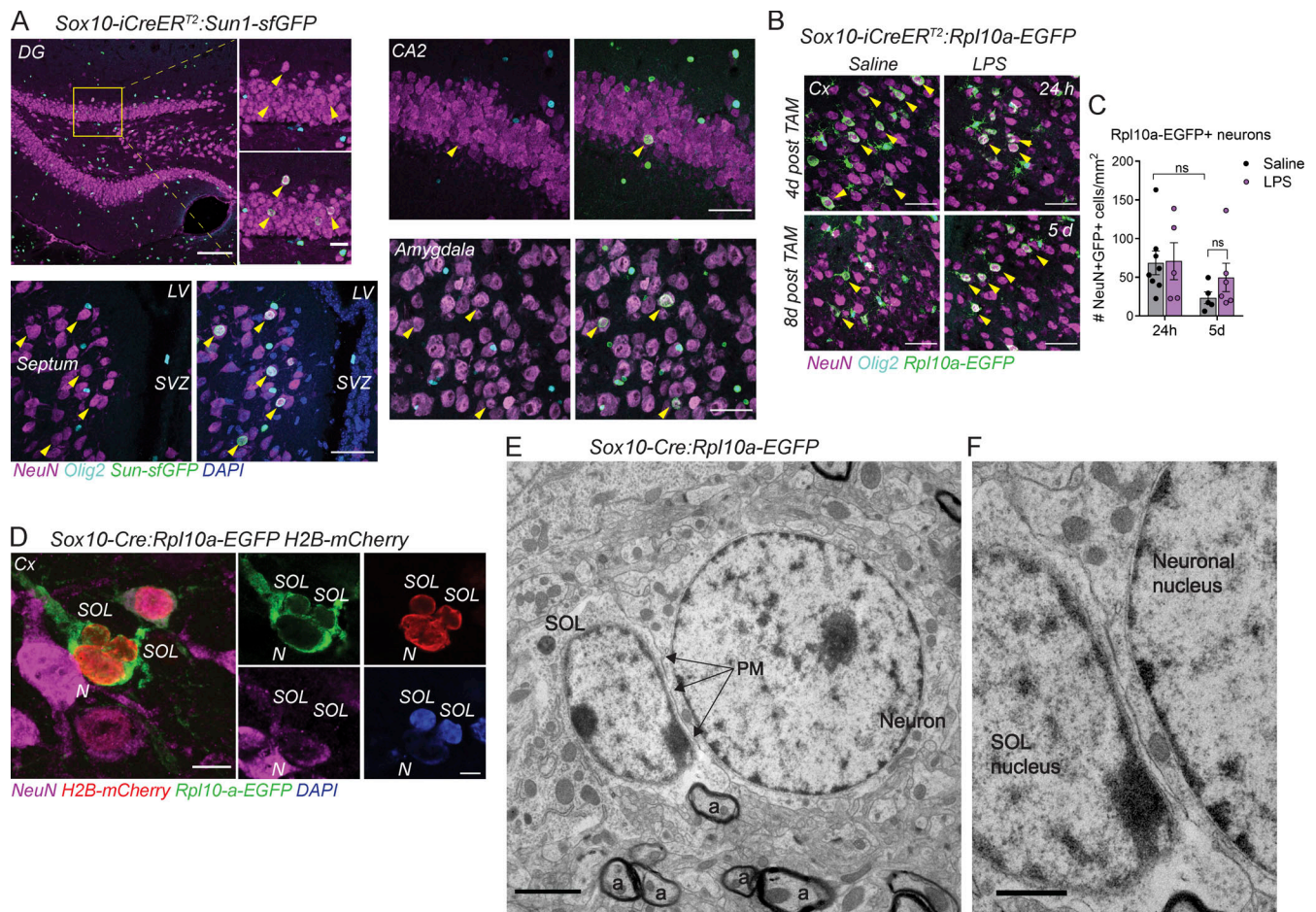https://doi.org/10.1084/jem.20221632

**Figure S3. SOL-neuron material transfer in the adult mouse brain. (A)** Reporter-positive neurons (arrowheads) in the hippocampal DG and CA2, septum, and amygdala of *Sox10-iCreER^T2^:Sun1-sfGFP* mice at 4 d after TAM. **(B)** Rpl10a-EGFP+ neurons (arrowheads) in the cortex of *Sox10-iCreER^T2^:Rpl10a-EGFP* mice at 24 h and 5 d after saline or LPS injection. **(C)** Quantification of Rpl10a-EGFP+ neurons in the cortex at 24 h and 5 d after LPS. **(D)** SOL-neuron nuclear pair immunoreactive for ribosomal Rpl10a-EGFP and histone H2B-mCherry in the cortex of adult *Sox10-Cre:Rpl10a-EGFP H2B-mCherry* mouse. Note, dense DAPI-labeled nuclei of SOL and diffuse DAPI-labeled neuronal nucleus. **(E and F)** TEM images of SOL-neuron pair with intact plasma membrane (PM) between nuclei. Multiple myelinated axons (a) are positioned close to SOL-neuron pair. All data are presented as mean ± SEM. Each circle represents an individual animal. P value was determined by one-way ANOVA with Bonferroni post hoc test. ns, $P > 0.05$. Data are representative of two (D), three (A–C), and four (E and F) independent experiments. Scale bar: 100 μm for DG in A and 20 μm for its enlargement; 50 μm for CA2, amygdala, and septum in A and for B; 10 μm for D and 5 μm for enlargement in D; 2 μm for E; and 1 μm for F. CA, cornu ammonis; Cx, cortex; LV, lateral ventricle; N, neuron; ns, not significant; SVZ, subventricular zone.

Video 1. **SOL-neuron nuclear pair in the adult mouse brain.** Animation through Z-stack obtained by super-resolution confocal imaging of reporter-positive Olig2+ SOL-neuron nuclear pair in the cortex of *Sox10-iCreER^T2^:Sun1-sfGFP* mouse 4 d after TAM injection. Olig2 (magenta), inner nuclear membrane reporter Sun1-sfGFP+ (green). Data are representative of two independent experiments. Frame rate: 23.98 frames/s.